

This work was written as part of one of the author's official duties as an Employee of the United States Government and is therefore a work of the United States Government. In accordance with 17 U.S.C. 105, no copyright protection is available for such works under U.S. Law.

CC0 1.0 Universal (CC0 1.0)

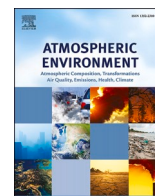
Public Domain Dedication

<https://creativecommons.org/publicdomain/zero/1.0/>

Access to this work was provided by the University of Maryland, Baltimore County (UMBC) ScholarWorks@UMBC digital repository on the Maryland Shared Open Access (MD-SOAR) platform.

Please provide feedback

Please support the ScholarWorks@UMBC repository by emailing scholarworks-group@umbc.edu and telling us what having access to this work means to you and why it's important to you. Thank you.



Influence of the transported Canadian wildfire smoke on the ozone and particle pollution over the Mid-Atlantic United States

Zhifeng Yang^{a,b,*}, Belay Demoz^{a,b}, Ruben Delgado^{a,b}, John Sullivan^c, Andrew Tangborn^b, Pius Lee^d

^a University of Maryland, Baltimore County, 1000 Hilltop Circle, Baltimore, MD, 21250, USA

^b Joint Center for Earth Systems Technology, 5523 Research Park Drive Suite 140, Baltimore, MD, 21228, USA

^c Atmospheric Chemistry and Dynamics Laboratory, NASA Goddard Space Flight Center, Greenbelt, MD, 20771, USA

^d NOAA Air Resources Laboratory (ARL), NOAA Center for Weather and Climate Prediction, 5830 University Research Court, College Park, MD, 20740, USA

HIGHLIGHTS

- Model simulations and satellite observations resolved the Canadian wildfire smoke transport path from Canada to the Mid-Atlantic region.
- The transported smoke enhanced the local O₃ and PM pollution over Mid-Atlantic region.
- Smoke particles intruded into the boundary layer at the altitude of 3.5 km.
- The O₃ vertical distribution increased from the surface to 1.5 km then decreased.

ARTICLE INFO

Keywords:

Canadian wildfire
Smoke
Ozone
Particulate matter
Mid-Atlantic
Planetary boundary layer

ABSTRACT

The integration of observations and models can improve air quality forecasts (in particular ozone (O₃) and particulate matter (PM)) for extreme events (e.g., wildfires). We present our work on the Canadian wildfire event on 6–12 June 2015 that impacted the air quality in the Mid-Atlantic region in the U.S. We use the Weather Research and Forecasting model coupled with Chemistry package (WRF-Chem), and various measurements from both ground-based and spaceborne observations, including the U.S. Environmental Protection Agency (EPA) AirNow data, the National Aeronautics and Space Administration (NASA) operated TROPOspheric Ozone lidar (TROPOZ), wind radar profiler, ceilometer, Moderate Resolution Imaging Spectroradiometer (MODIS), Cloud-Aerosol Lidar with Orthogonal Polarization (CALIOP). The objective is to understand the physics of the Planetary Boundary Layer (PBL) and its role on the O₃ and PM forecast. The findings show that the model captured the O₃ diurnal variation and PM spatial distribution both horizontally and vertically by comparing with EPA AirNow and MODIS/CALIOP observations, respectively. Wildfire smoke was transported from central Canada through Lake Michigan, passing the Ohio River Valley and down to the Baltimore-Washington D.C. metropolis. The nighttime O₃ mixing ratio reached 30 ppbv, while the daytime O₃ mixing ratio approached larger than 100 ppbv near AirNow stations in Maryland, due to the mixing of the transported smoke into the PBL. The novel NASA TROPOZ lidar at Beltsville resolved the O₃ vertical profile and the ceilometer identified the smoke intrusion at altitudes above 3.5 km, but later mixed down into the PBL and surface which was also resolved by the model. Thus, integrating both model and observations from different platforms confirms the Canadian wildfire source and transport pathway and improves the understanding of the air quality forecast during the extreme wildfire event.

1. Introduction

Wildfires influence ozone (O₃) and particulate matter (PM), which play vital roles in air quality, climate change, and human health

(Intergovernmental Panel on Climate Change (IPCC), 2013). Wildfires burned from forest, savanna and grassland, caused by lightning and/or humans (prescribed burns or accidents), are sources of both primary and secondary pollutants (trace gases and aerosol particles) (Crutzen et al.,

* Corresponding author. University of Maryland, Baltimore County, 1000 Hilltop Circle, Baltimore, MD, 21250, USA.

E-mail address: zhifeng.yang@umbc.edu (Z. Yang).

<https://doi.org/10.1016/j.atmosenv.2022.118940>

Received 14 June 2021; Received in revised form 15 December 2021; Accepted 4 January 2022

Available online 14 January 2022

1352-2310/Published by Elsevier Ltd.

1979; Crutzen and Andreae, 1990; Andreae and Merlet, 2001). The volatile organic compounds (VOCs) and nitrogen oxides (NOx) released from wildfires form O₃ in the troposphere, by photochemical reactions in the presence of sunlight (Val Martin et al., 2006; Jaffe and Wigder, 2012). Long-term exposure to high concentrations of O₃ leads to health issues, i.e., irritates lungs, aggravates bronchitis, emphysema, and asthma (Lippman, 1991; Gan et al., 2020). PM_{2.5} has been associated with increased morbidity and mortality from cardiorespiratory diseases and cancers (Chen et al., 2020; Hao et al., 2015). Recent studies show that even exposure to low concentrations of PM_{2.5} adversely affects human organ systems (Chen et al., 2016; Power et al., 2016). The Global Burden of Disease Study (2017) shows ~4 million premature deaths annually are resulted from the exposure of PM_{2.5} (Stanaway et al., 2018). The subject of this study is becoming increasingly important because future trend of wildfire events, the frequency and averaged area burned each year is predicted to increase due to warmer, drier climate (Liu et al., 2010; Schoennagel et al., 2017). Climate change is expected to increase the wildfires occurrences over the regional and/or global scale. Thus, long-term smoke transport effects on human health increases are likely. Estimates are that global warming has already impacted the frequency and intensity of wildfires for Canadian and U.S. forests over the past century (Gillett et al., 2004; Westerling et al., 2006; Roberts et al., 2020).

The long-range transport of smoke and its contribution to local air pollution is difficult to quantify and thus forecast (Kunzli et al., 2006; Wu et al., 2018). The physics of how the long-range transported smoke mixes into the boundary layer from the upper troposphere is not well understood. Satellite observations of such long-range transport smoke is readily available, which help the modeling of physical processes on how the long-range transported smoke mixes down to the surface (Yang et al., 2013; Campell et al., 2016). The synoptic setting, the physical development and dynamics of wildfires from the local-to-regional scales govern how the smoke transport impacts downwind regions at the local pollution scale.

A number of previous studies have investigated the influence of Canadian boreal forest wildfires on trace gases and particles (Wotawa and Trainer, 2000; McKeen et al., 2002; Colarco et al., 2004; DeBell et al., 2004; Morris et al., 2006). An extensive wildfire event, which occurred over northwestern Canada in June 1995, resulted in the enhancement of CO and O₃ concentrations over the midwestern and eastern U.S. (Wotawa and Trainer, 2000; McKeen et al., 2002). Both models and observations showed that O₃ concentration increased by 15–18% over the eastern U.S., due to both photochemistry and transport (Wotawa and Trainer, 2000). The O₃ production is sensitive to the NOx/CO ratio in the fire emission, which is highly uncertain and variable (McKeen et al., 2002). A molar NOx/CO ratio of 0.007 yields model comparisons that are most consistent for O₃ and ΔO₃/ΔCO observations within aged fire plumes. For this NOx/CO emission ratio, and considering the entire eastern U. S., most of the O₃ increase is associated with the NOx emitted directly by the fires and the photochemical O₃ formation that occurs before the plumes actually reach the U. S. In addition, the effectiveness of emission controls also depends on the photochemical regime of O₃ formation, namely, whether production is NOx limited or VOC limited. In the VOC-limited (or NOx-saturated) regime, VOC emission reductions reduce the chemical production of organic radicals (RO₂), which in turn lead to decreased cycling with NOx and consequently lower concentration of O₃ (Milford et al., 1989). Another Canadian wildfire happened in Quebec, Canada early July 2002 (Colarco et al., 2004; DeBell et al., 2004; Morris et al., 2006). Smoke and other pollutants were transported to the U.S. at low altitudes behind advancing cold fronts (Colarco et al., 2004). The significant enhancements of CO, PM_{2.5}, organic and black carbon (OC and BC), and the soluble aerosol species NO₃⁺, Ca²⁺, and the biomass burning tracer K⁺ marked this wildfire event. The study reported that the smoke plumes were transported to New England, which depended on a combination of factors, among which are the altitude of transport, the degree of

enhancements and chemical composition of aerosols varied with sampling station elevation and latitude (DeBell et al., 2004). Overall, these studies utilized a variety of observations and models to explore the origin of Canadian wildfires and their impacts on the U.S. air quality.

An example of the effect of long-range transport Canadian wildfire smoke in June 2015 and its effect on air quality was reported by Dreesen et al. (2016), which investigated the wildfire influence on the local air quality on 9–12 June 2015 from the policy makers' perspective. They studied the impacts of this Canadian wildfire on BC, OC, O₃ and PM concentrations in Maryland from in-situ and remotely sensed measurements obtained from the Maryland Department of Environment. However, it only mentioned the underestimation of O₃ forecasts from the NOAA operational Community Multiscale Air Quality Modeling System (CMAQ), due to no Canadian wildfire information included, without further analysis. Following this report, Sullivan et al. (2017) reported a focused study on the lesser-characterized night-time transport and vertical mixing/entrainment of O₃ in the context of "next-day" O₃ exceedances. They studied how the nocturnal low-level jet (NLLJ) impacted the transport of O₃ by employing NASA TROPOZ DIAL ozone lidar, radar wind profilers, radiosonde, ozonesonde on 11–12 June 2015. They also used WRF model simulation (without chemistry) to explore the horizontal range of NLLJ, and forward trajectories to track in which direction that NLLJ advected the O₃ contaminated air. They showed the contaminated nocturnal residual layer (RL) with O₃ mixing ratio between 70 and 100 ppbv near 1 km over the surface. Advection of NLLJ and entrainment of the polluted RL. The radar wind profiler observations show that the NLLJ transported the O₃ contaminated air out of the Baltimore-Washington region. Although these two studies described the pollution episode caused by the Canadian wildfires at the local region in Maryland, a coordinated mesoscale model-assisted study of this event had not been performed to date. Neither of them investigated this Canadian wildfire from the beginning of the event and rarely employed the air quality model. In this work, we examine this impactful Canadian wildfire event by combining the advanced ground-based in-situ and remote sensing observations, together with the Weather Research and Forecasting model coupled with Chemistry package (WRF-Chem) to explore the smoke transport path and validate its impact on the local-to-regional air pollution. These include details of the arrival of the transported smoke, the satellite-model comparisons, the regional surface and remote sensed measurements and in particular the evolution of measurements and model simulations within the Planetary Boundary Layer (PBL).

The scientific questions to be resolved are as following. 1). What is the smoke transport pathway and how did meteorology influence its transport? (satellite & model) 2). What's the contribution of smoke to the local O₃ pollution? (radar wind profiler, AirNow diurnal variation) 3). How smoke intruded into the boundary layer and mixed? (ceilometer & model) 4). What's the vertical profile of the smoke-enhanced O₃? 5). How does the model perform on simulating O₃ spatiotemporal distribution? This paper follows the following structure. First, we set up the study domain and model configuration, including the parameterization schemes and designed model experiments. Second, a description of the standard surface and upper-air O₃ data, ground-based remote sensing data, and satellite data employed in the analysis, followed by the results and discussion section. The result analysis includes smoke large-scale transport and local O₃ and PM enhancement due to smoke. Finally, we complete this study with a conclusion.

2. Model configuration and experiment design

2.1. Model configuration and emissions

2.1.1. Model configuration

WRF-Chem version 3.9 has the air quality components consistent with the meteorological components (Grell et al., 2005; Fast et al., 2006). In this study, the urban canopy scheme used is the urban canopy

model (UCM) with 4-category UCM option with surface effects for roofs, green roofs, walls, and streets (Kusaka et al., 2001). This UCM is the only urban canopy scheme option available in WRF-Chem version 3.9, since the PBL scheme used is Yonsei University scheme (YSU, Hong et al., 1996, 2006). An extended discussion of the different model PBL parameterization schemes and their success in comparison with lidar observed PBL data in this study region is reported by Lopez-Coto et al. (2020). The land-surface model scheme is the Noah Land Surface Model (Chen and Dudhia, 2001). The cumulus scheme is the Kain-Fritsch scheme (Kain and Fritsch, 1990; Kain, 2004). The cloud microphysics scheme is the New Thompson et al. scheme with ice, snow and graupel processes suitable for high-resolution simulations (Thompson et al., 2004). Model radiation treatment utilizes the Rapid Radiative Transfer Model for General Circulation Models short-wave and long-wave radiation schemes (RRTMG, Iacono et al., 2008), including the aerosol radiation feedback. The gas-phase chemistry and aerosol module employ the Carbon Bond Mechanism-Version Z (CBM-Z, Zaveri and Peters, 1999) and Model for Simulating Aerosol Interactions and Chemistry (MOSAIC, Zaveri et al., 2008), respectively. The photolysis scheme is the Fast-J scheme (Fast et al., 2006).

The model study area includes southern Canada and the contiguous U.S. to cover the wildfire source region (Saskatchewan, Canada) and smoke transport paths (indicated by the yellow line in Fig. 1) and provide lateral boundary conditions for the nested domains. This outer domain is further resolved by two nested regions that progressively focus and center at the local study region, Baltimore-Washington, D.C. metropolis. Thus, three domains are established with the spatial resolution of 27 km (d01) and two nested domains at 9 km (d02) and 3 km (d03), respectively. The first nested domain (d02) is designed to capture the path of the smoke transport through the Great Lakes and the Ohio River Valley which borders the study region in the immediate Northeast and on the path of several space lidar data transect observations used for comparison. The second nested domain (d03) is selected to allow for focused and detailed comparisons with air quality investigation and observation over the Baltimore-Washington, D.C. metropolis. The model vertical grid uses 65 levels with a model top at 100 hPa and about 35 levels were set below 700 hPa, in order to provide model output that would resolve the PBL.

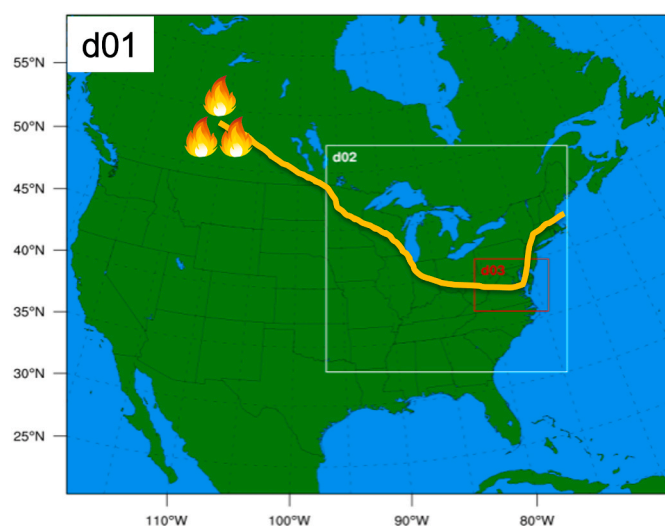


Fig. 1. WRF-Chem study area with outer domain (southern Canada and the contiguous U.S.) two nested domains (white rectangle (d02) and red rectangle (d03)). The fire icons indicate the wildfire source locations and the yellow line indicates the approximate smoke transport path as can best be deduced from satellite observations. (For interpretation of the references to color in this figure legend, the reader is referred to the Web version of this article.)

2.1.2. Emission data sets

All the emission data sets used in this study are listed in Table 1. Wildfire emissions are the Fire INventory from NCAR (FINN, Wiedinmyer et al. 2006, 2011). It is retrieved from satellite observations (Moderate Resolution Imaging Spectro-radiometer, MODIS) of active fires and land cover, together with emission factors and estimated fuel loadings to provide daily, 1-km resolution open burning emissions estimates. Anthropogenic emissions are from the 2011 National Emission Inventory (NEI2011), which is a comprehensive and detailed estimate of the air emissions for criteria pollutants, precursors, and hazardous air pollutants. It includes point sources and area sources with resolution of 4 km, covering all the 48 contiguous states as well as selected regions of Canada and Mexico. Biogenic emissions are from the Model of Emissions of Gases and Aerosols from Nature (MEGAN), which is a modeling system for estimating the net emission of gases and aerosols from terrestrial ecosystems into the atmosphere (Guenther et al., 2006). It is driven by land cover, weather, and atmospheric chemical composition and has 1 km resolution globally.

NEI emission is the emission from a typical summer day. To employ the optimal anthropogenic emissions, NEI2005 and NEI2011 are compared over the second nested domain (Fig. 2). Here we show the NO emission flux rate from NEI2005 and NEI2011, and notice the difference over the Chesapeake Bay. NEI2011 takes the ship emissions into account, while NEI2005 does not. Thus, we employ NEI2011 in the following model simulation experiments.

2.1.3. Smoke modeling

After being emitted from the wildfire, the smoke was lifted via positive buoyancy, driven by the fire radiative power as described in Peterson et al. (2013) and Freeborn et al. (2014). Associated physics, due to radiative cooling combined with efficient heat transport by convection, led to a rapid decay of temperature above the burning area. The WRF-Chem model simulates this process in which smoke emissions are lifted to a certain vertical model level due to heat flux (Grell et al., 2011). In the WRF-Chem plume rise module, land cover types include tropical forest, boreal forest, Cerrado (or woody savanna), and grassland (or cropland), each of which has its own minimum and maximum heat fluxes. For example, boreal forest has the minimum and maximum heat fluxes of 30.0 kW m^{-2} and 80.0 kW m^{-2} , respectively. Thus, the plume injection height in the model is determined by a combination of factors including the land cover types, their fractions in each model mesh, and burned area.

2.2. Experiment design

In order to stabilize the meteorological and chemical fields and capture the whole smoke transport pathway, all the experiments were conducted from 0000 UTC, 3 June to 0000 UTC, June 14, 2015. The first 3-day simulations were treated as spin-up, and the remaining simulations (from 0000 UTC, 6 June to 0000 UTC, 14 June) were selected for analysis. The smoke particle arrived at the Great Lakes on 8 June and the Mid-Atlantic region on 9 June, while smoke induced O_3 exceedance occurred on 11–12 June. Thus, the end simulation period was 14 June.

Table 1
Emission data sets as inputs of WRF-Chem.

Dataset	Full Name	Resolution (H)	Parameters	Availability
FINN	Fire Inventory from NCAR	$1 \times 1 \text{ km}^2$ hourly	CO , CO_2 , NO_x , SO_2 , PM , OC , BC , and VOC species	2002–2020
NEI2011	National Emission Inventory (2011)	$4 \times 4 \text{ km}^2$ hourly	CO , NO_x , SO_2 , PM , OC , BC , and VOC species	2011

H: Horizontal

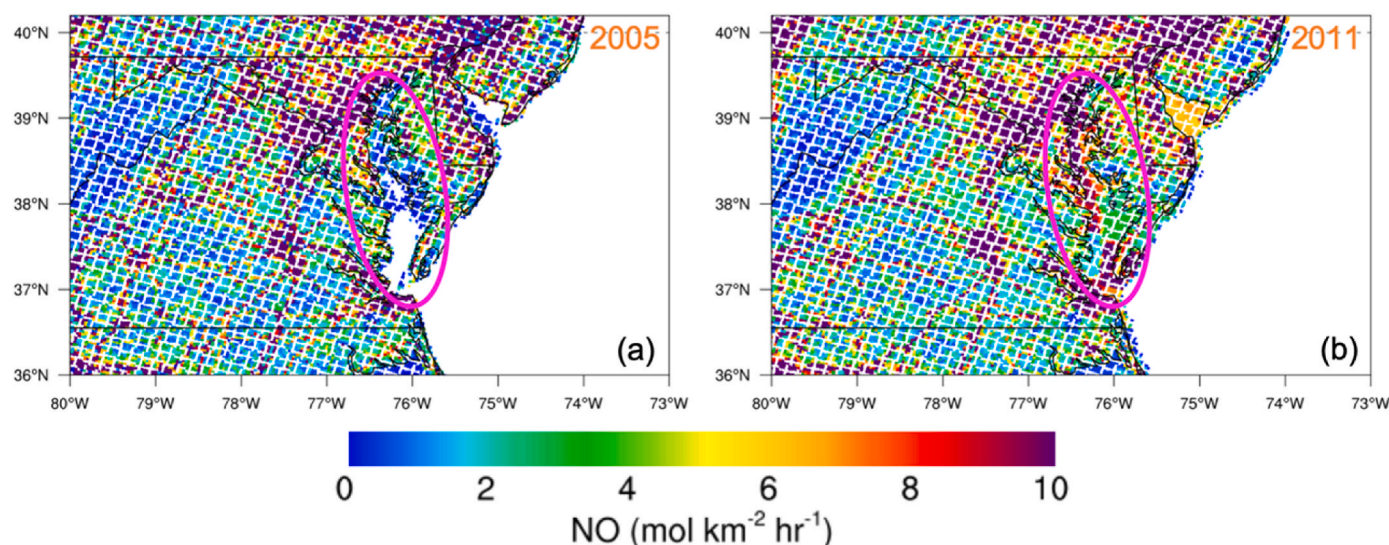


Fig. 2. (a) NO emission flux rate of NEI2005. (b) NO emission flux rate of NEI2011. The Chesapeake Bay is shown in the pink ellipse. (For interpretation of the references to color in this figure legend, the reader is referred to the Web version of this article.)

Three numerical experiments were performed to investigate and quantify the impacts of different emissions (Table 2). The first numerical experiment (Ex1) is designed to quantify the anthropogenic and biogenic emission influence on O_3 and PM. This experiment helps us understand the O_3 and PM pollution without the transported Canadian wildfire smoke. The second numerical experiment (Ex2) is conducted with only fire emissions to quantify the contribution of the Canadian wildfire smoke to the elevated O_3 and PM pollution in the Mid-Atlantic region. The third numerical experiment (Ex3) includes anthropogenic, biogenic, and fire emissions, to evaluate the model performance with observations, since this is the closest situation to reality.

3. Data

The local impacts of the Canadian wildfire are demonstrated using observations from the ground-based in-situ and remotely sensed instruments mentioned below. The site locations are shown in Fig. 3 which also shows the terrain height in the gray contour. The data availability in each site is shown in Table 3. The dot color of each site in Fig. 3 shows the available observations as listed in Table 3. The Beltsville site is the super observation site which has all the instruments used in this study, e. g., 915 MHz radar wind profiler, AirNow O_3 , ceilometer, TROPOZ DIAL ozone lidar, and ozonesonde.

A summary of the observation data used in this study is given in Table 4 followed by a brief explanation of each data set.

3.1. Standard surface and upper air O_3 data

The U.S. Environmental Protection Agency (EPA) collects observation data from a network of surface O_3 and PM monitoring and detection

Table 2

Experiments designed to quantify the emission influences on the air quality.

Experiment	Biogenic emission	Anthropogenic emission	Fire emission	Purpose
Ex1	MEGAN	NEI2011	N/A	anthropogenic and biogenic emission influences
Ex2	N/A	N/A	FINN	fire emission influences
Ex3	MEGAN	NEI2011	FINN	anthropogenic, biogenic, and fire emission influences

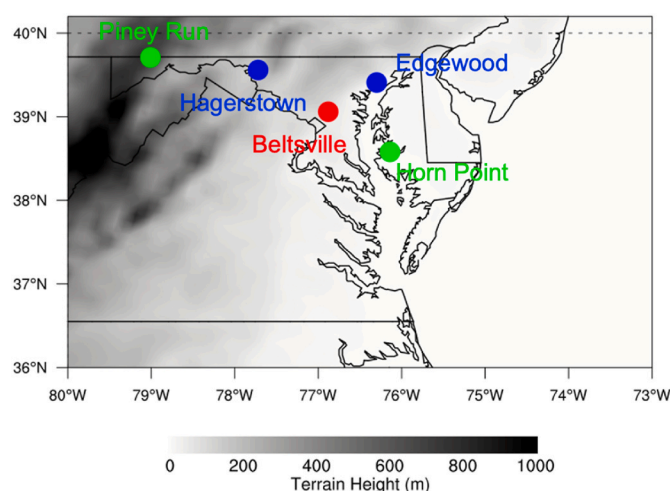


Fig. 3. Terrain height in the Mid-Atlantic region, overlaid with the site locations.

that covers a large spatial region within the U.S. in the last few decades (Dye et al., 2004). The EPA's AirNow program provides real-time forecast and observed surface air quality information across the U.S. over 1000 monitoring stations. AirNow data from surface stations in Maryland within the inner nested domain (d03) is used for the surface validation of the WRF-Chem model simulation.

Ozonesonde relies on the oxidation reaction of O_3 with potassium iodide in solution launched by the Howard University Beltsville Campus routinely (HUBC, 39.06°N, 76.87°W, 52 m above sea level, Komhyr et al., 1995). Ozonesonde observed O_3 vertical profiles resolve the O_3 vertical distribution and evaluate model simulated O_3 vertical distribution.

3.2. Ground-based remote sensing data

This work uses data from wind radar: 915 MHz radar wind profiler, and two ground-based lidars: the NASA Goddard Space Flight Center TROPOspheric OZone Differential Absorption Lidar (TROPOZ O_3 lidar; Sullivan et al., 2015) and a Vaisala Ceilometer CL51. During the employment, the TROPOZ and CL51 were operated from HUBC.

Table 3
Site information used in this study.

Site	Latitude (°)	Longitude (°)	Elevation (m)	Measurements available
Beltsville	39.06	-76.88	52	1, 2, 3, 4, 5
Edgewood	39.41	-76.30	8	2
Hagerstown	39.56	-77.72	161	2
Horn Point	38.58	-76.14	2	1
Piney Run	39.71	-79.01	763	1

1: 915 MHz radar wind profiler, 2: AirNow O₃, 3: ceilometer, 4: TROPOZ DIAL ozone lidar, 5: ozonesonde.

Table 4
Observation data sets used in this study.

Dataset	Full Name	Spatial & Temporal Resolution	Parameters	Availability
AirNow	EPA AirNow	hourly (H)	O ₃ , PM _{2.5} , PM ₁₀ , SO ₂ , CO, NO ₂ , VOC, NOx, NOy, lead, pressure, temperature, relative humidity, wind	1980–2020
Ozonesonde			O ₃ mixing ratio, O ₃ partial pressure, altitude, water vapor mixing ratio, relative humidity, pressure, and temperature	Jun 12, 2015
915 MHz radar wind profiler		60 m (V) 5–6min	Wind, temperature,	Jun 2015
TROPOZ DIAL	TROPOspheric OZone Differential Absorption Lidar	15 m (V) 6min	O ₃ mixing ratio, pressure, temperature	10–12 Jun 2015
Vaisala Ceilometer CL51		15 m (V) 15s	Attenuated backscatter, Cloud base height, Cloud depth	10–12 Jun 2015
MODIS	Moderate Resolution Imaging Spectro-radiometer	1 × 1 km ² (H)	AOD	Dec 1999–Now (Terra) May 2002–Now (Aqua)
CALIOP	Cloud-Aerosol Lidar with Orthogonal Polarization	5 km (H), −0.5–8.2km/ 30 m (V)	Extinction Coefficient, Vertical Feature Mask	Jun 2006–Now

H: Horizontal; V: Vertical.

The 915 MHz radar wind profiler provides measurements of wind and precipitation profiles through the boundary layer. With the radio acoustic sounding system (RASS), it can also measure virtual temperature (Ecklund et al., 1988). The Maryland Department of Environment operates radar wind profiler and radio acoustic sounding systems over three sites, Horn Point, HUBC, and Piney Run. The 915 MHz radars have two models, DeTect RAPTOR DBS-BL/LAP-3000 Upgrade profilers (Piney Run and Beltsville) and DeTect RAPTOR VAD-BL profiler (Horn Point). These radar wind profiler measurements begin at about 100 m above ground level (AGL) up to about 2500 to 4000 m AGL in the atmosphere. In general, radar wind profilers function by sending out radio waves at fixed levels into the atmosphere along each of its antenna's beam directions. Small amounts of the signal are then scattered back to the antenna. Wind speed and direction are computed by determining the Doppler frequency shift.

The radar wind profiler data is missing at 0.6 km and 1.3 km at Piney Run and Beltsville, and 1.6 km at Horn Point. The Piney Run station is located in the rural area over a mountain range in the Appalachian Mountains. The HUBC station is located in the suburban area between Baltimore and Washington D.C., and the western shore of the Chesapeake Bay. While the Horn Point station is in the coastal area at the eastern shore of the Chesapeake Bay (Fig. 3).

The TROPOZ O₃ lidar has been developed in a transportable trailer to take routine measurements of tropospheric O₃ (Sullivan et al., 2015). The laser wavelength is 289 nm and pulse frequency is 6 s to measure the absorption cross section and retrieve the O₃ mixing ratio vertical profile whose vertical resolution is 15 m. Its O₃ vertical profile extends from the surface to 12 km. But this study only employs TROPOZ O₃ profiles from 0.1025 km to 2.5 km, where its data are available. In addition, TROPOZ O₃ lidar is a part of the ground-based Tropospheric Ozone Lidar

NETwork (TOLNET) which is designated to improve the current number of tropospheric O₃ profiles (Newchurch et al., 2016; <https://www-air.larc.nasa.gov/missions/TOLNet/>). In this study, TROPOZ O₃ profiles are used to resolve the O₃ profile temporal evolution and evaluate model simulated O₃ vertical distribution.

Vaisala Ceilometer CL51 is designed to measure the aerosol backscatter profile from the lower atmosphere and reach up to cirrus cloud heights. It uses a low power indium gallium arsenide laser diode (InGaAs) laser at the wavelength of 910 nm and is primarily used for cloud base reporting with its range reaching up to 13 km. It is one of the candidate instruments for mixed layer height detection and reporting over EPA's Photochemical Assessment Monitoring Stations (PAMS, Caicedo et al., 2020). CL51 backscatter profile observations have been used to study the evolution of the PBL and indicator for air mass change associated with atmospheric dynamics (Carroll et al., 2019). In this study, Ceilometer CL51 data is used to indicate the approximate range of the transported wildfire smoke and its mixing down to the surface as well as to visually indicate the PBL height (PBLH) evolution.

3.3. Satellite-based data: AOD and VFM profile

The MODIS instruments aboard Terra (launched in December 1999) and Aqua (launched in May 2002) satellites measure spectral radiance in 36 channels, with resolutions ranging from 250 m to 1 km at nadir. Three of these channels (470 nm, 660 nm, and 2130 nm) are used to retrieve standard AOD, which is interpolated in the mid-visible spectrum (550 nm). MODIS AOD is reported to have an uncertainty of $\pm (0.05 + 0.15\tau)$ over dark land and $\pm (0.04 + 0.10\tau)$ over ocean, where τ is the MODIS retrieved AOD (Levy et al., 2015). In this work, MODIS aerosol Level 2 Collection 6.1 products (MOD_04 and MYD_04 from Terra and

Aqua, respectively) are used to track the large-scale smoke transport and compare with model simulations.

The Cloud-Aerosol Lidar with Orthogonal Polarization (CALIOP) is a two-wavelength polarization active lidar aboard the CALIPSO satellite (Cloud-Aerosol Lidar and Infrared Pathfinder Satellite Observations, Winker et al., 2009). CALIOP performs global profiling of aerosols and clouds in the troposphere and lower stratosphere. CALIOP Level 2 processing involves separating the aerosol and cloud layers followed by determining the aerosol types (smoke, polluted dust, clean continental, polluted continental, dust, and clean marine) and cloud ice-water phase (Liu et al., 2004, 2009; Omar et al., 2009; Winker et al., 2009). CALIOP vertical feature mask vertical resolutions are as below. -0.5 to 8.2 km is 30 m. 8.2 – 20.2 km is 60 m. 20.0 – 30.1 km is 180 m. CALIPSO is on A-train. It passes the same location twice a day, at $1:30$ a.m. and $1:30$ p.m. local time. The CALIPSO orbit is controlled to keep cross-track errors with respect to the 16-day grid less than ± 10 km (Winker et al., 2009). The CALIOP Vertical Feature Mask (VFM) Level 2 products are selected to track the smoke vertical distribution and evaluate model vertical profile simulations of the aerosol mass concentration.

4. Results

4.1. Case description: wildfire event of 6–8 June 2015

This case is a long-range transported smoke generated by wildfires over the western Canada. This Canadian wildfire event was ignited by lightning at the southwest of the Great Slave Lake and south of the Lake Athabasca in the Alberta and Saskatchewan Provinces on June 6, 2015 (Canadian Interagency Forest Fire Centre [CIFFCC], 2020). Abnormally warm and dry weather readily resulted in conditions that favor lightning-induced wildfire over the boreal forest in Canada (Dreessen et al., 2016).

The Canadian wildfire lasted for three days from 6–8 June 2015. To better illustrate the fire emission, the 1 km resolution FINN fire emission flux rate was aggregated to 100 km by averaging them using equation (1).

$$\bar{F}_j = \frac{\sum_{i=1}^N F_i}{N} \quad (1)$$

Where \bar{F}_j is the average flux rate within the j th 100 km by 100 km grid. N is the total number of 1 km by 1 km grids within a 100 km by 100 km grid. F_i is the flux rate in a 1 km by 1 km grid.

The total area density (or mass per area) was calculated based on the flux rate in each hour by following equation (2) below

$$\rho_A = \sum_{j=1}^n \bar{F}_j * t \quad (2)$$

Where ρ_A is the area density. F_j is the flux rate, and $t = 3600$ s, is the total seconds in 1 h. The total $PM_{2.5}$ emission area density is about 60 – 80 $mg\ m^{-2}$ over the south of Lake Athabasca and exceeds 100 $mg\ m^{-2}$ over the west of Lake Winnipeg (Fig. 4b, d). In addition, the total fire size is 50 – 100 km^{-2} over the south of Lake Athabasca and 100 – 150 km^{-2} over the west of Lake Winnipeg. Other fire events, which could transport smoke to the study region, are not significant compared with the Canadian wildfire event on 6–8 June (Fig. 4a, c).

4.2. Long-range transport of fire-induced smoke

4.2.1. Smoke transport from the source to the study region

A combination of MODIS AOD and CALIOP VFM profile imagery as well as model simulations are used to diagnose and reveal the three-dimensional (3D) long-range transport path of the smoke from the source region to the U.S. The shortcomings of the polar-orbiting satellite imagery that are limited to only twice daytime snapshots daily are

augmented by the capability of model simulations with fine integral time intervals and output results from every hour to a few minutes. Careful analysis of these satellite images and model simulations revealed four key regions as the smoke was transported from Canada to the U.S. (not shown here): the source region, Lake Michigan, Ohio River Valley, and Mid-Atlantic and Northeast.

The spatial span of the wildfire source region was 105° W – 115° W and 55° N – 60° N, which included multiple fire events, leading to the tremendous amount of smoke emissions. At the time, the northwest prevailing winds and a cold front impacted the fire source region from the northwest advecting the smoke further southeast as can be seen in the daily weather maps available from NOAA (available at https://www.wpc.ncep.noaa.gov/dailywxmap/index_20150606.html).

The model simulation (Ex2) revealed that the enhanced surface $PM_{2.5}$ mass concentration contributed by smoke was about $15\ \mu g\ m^{-3}$ in Minnesota on 8 June (Fig. 5a, d, g). 9 June, the fire-induced smoke arrived at the Ohio River Valley, located over Indiana and Ohio. The surface west wind speed was $10\ m\ s^{-1}$ (Fig. 5b, e, h). Nevertheless, the wind direction shifted towards south at midnight on 10 June and lasted for 12 h before shifting back to southwest at noon on 10 June. Because of the wind shift, the smoke was trapped over the Ohio River Valley for more than one day, leading to the stagnant smoke and mixing with the local air pollutants. Despite both wet and dry deposition, the PM concentration kept stable and did not decrease much. On 10 June, the transported smoke arrived at the Mid-Atlantic region (Fig. 5c, f, i). An opposing flow from the southeast over the region blocked the smoke-filled air mass and concentrated it along a relatively narrow band region as observed on 11 June.

4.2.2. Evolution of the smoke-laden air vertical structure

CALIOP data was used to track the smoke vertical distribution as it was transported to the Mid-Atlantic region. The CALIOP VFM product which classifies aerosol types, e.g., smoke, dust, polluted dust, clean continental, polluted continental, and clean marine is shown in Fig. 6d–f. The black color indicates smoke.

The CALIPSO ground track passed over the southeast of Wisconsin and CALIOP detected the smoke in the afternoon of 8 June, around 0830 UTC (1330 CDT¹). The smoke transport path overlaid with the CALIPSO ground track is indicated with a pink line in Fig. 5g and as a pink bar in Fig. 6a and d. The smoke between 45° N and 50° N was about 5 km deep, similar to the simulation with FINN fire emissions (Ex2) results (Fig. 6a). In addition, the model simulation showed the continuous smoke vertical distribution along the CALIPSO ground track. As the smoke drifted further south into the U.S., with the bulk of it over the Mid-Atlantic, CALIOP showed very little smoke detected, primarily because clouds blocked detection of the smoke beneath (pink bar, Fig. 6e).

The CALIOP data intercepted the smoke layer as it passed Lake Michigan and arrived over the Mid-Atlantic showing a general “settling” of the smoke plume layer to about 3 km deep (pink bar, Fig. 6f). The model simulation captured the general vertical smoke transport compared with the CALIOP product, as well as the plume height (Fig. 6c).

4.3. Local O_3 and PM enhancement

4.3.1. Local wind profile evolution

Transport of the smoke plume in any numerical weather model primarily depends on the quality of the 3D wind simulations, at least on the average large-scale character. Small scale perturbations are not easy to reproduce by a regional model. The simulated vertical wind profile is evaluated using 915 MHz wind radar profiler observations. Fig. 7 shows the observed and simulated vertical wind profiles on 8–12 June at Piney Run, Beltsville, and Horn Point whose locations are shown in Fig. 3.

¹ CDT: Central Daylight Time, CDT = UTC - 5:00.

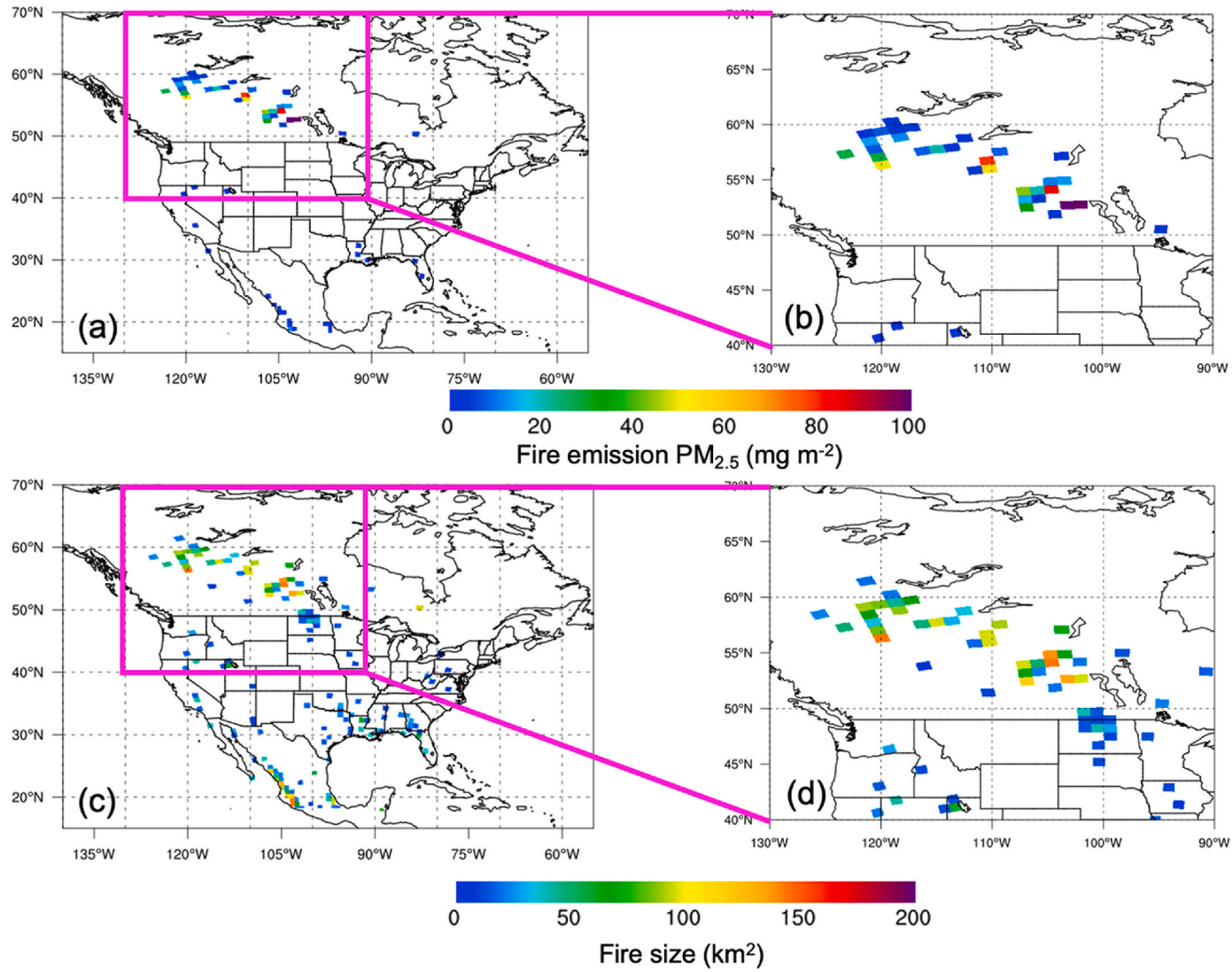


Fig. 4. (a) total $PM_{2.5}$ mass flux rate from FINN fire emissions over North America on 6–8 June 2015. (b) $PM_{2.5}$ mass flux rate from FINN fire emissions over the western Canada. (c) mean fire size from FINN fire emissions over North America on 6–8 June 2015. (d) mean fire size from FINN fire emissions over the western Canada. The grid spacing resolution is $100\ km \times 100\ km$.

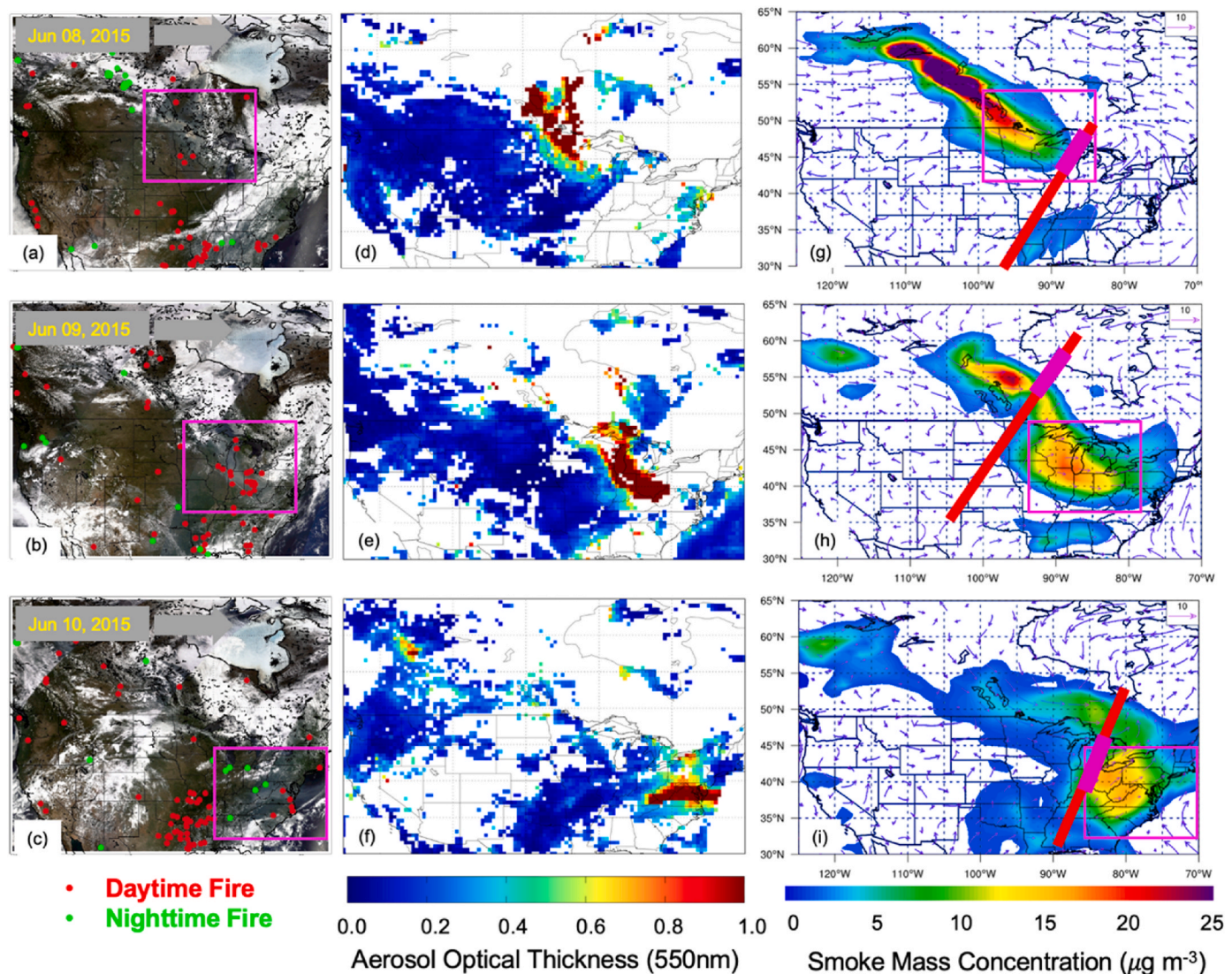


Fig. 5. Panels (a–c): MODIS three-band color overlay images (band 1—red, band 4—green, and band 3—blue) from Terra on 8, 9, and June 10, 2015. Red and green dots indicate the locations of fires detected by MODIS at daytime and nighttime, respectively. Panels (d–f): MODIS AODs at 550 nm. Panels (g–i): WRF-Chem simulated surface PM_{2.5} mass concentration (Ex2). The pink rectangles indicate where the smoke front is. (For interpretation of the references to color in this figure legend, the reader is referred to the Web version of this article.)

Also, shown are the observed vertical wind profile differences between Beltsville and Horn Point (Fig. 7g).

The wind speed at three stations appeared low near the surface and increased with altitude, from 10.0 m s⁻¹ at 0.3 km to over 20.0 m s⁻¹ at 2.0 km on 8–9 June, which was NLLJ. The NLLJ advected pollutants to the downwind region. Starting late 9 June, the wind speed further decreased to 2.0–4.0 m s⁻¹ from the surface to 2.0 km. This decrease was pronounced over Beltsville and Horn Point veering from south near the surface to west aloft. The wind speed followed significant diurnal variations, with low wind speed near 0000 UTC and high wind speed at 0600 UTC. The overall wind direction was west, shifted to south close to the surface on 8–12 June, and this is the reason that the fire smoke was advected from the Mid-Atlantic region to the Northeast.

The wind direction at Beltsville was south near the surface while shifted to west above 0.6 km. Its wind speed was lower than Piney Run, while they had similar wind patterns (Fig. 7c and d). The strongest wind happened on 8 June, with relatively low wind speed around 10.0 m s⁻¹ from surface to 0.3 km and reached 20.0 m s⁻¹ at higher levels. Other than that, the wind speed was around 10.0–12.0 m s⁻¹ on 10–12 June. Its wind speed diurnal variation was similar to Piney Run.

The wind direction at Horn Point was south near the surface and shifted slightly to west above 0.3 km (Fig. 7e and f). Its wind speed was lower than Piney Run and Beltsville on 8 June. While it had stronger wind afterwards, due to the contribution of the south wind over the Chesapeake Bay. It also maintained the wind speed diurnal variation but with smaller wind speed contraction between daytime and nighttime. This was caused by the water body over the Chesapeake Bay. The high relative heat capacity of water kept the surface temperature change smaller than the land surface between daytime and nighttime.

The vertical wind profile differences between Beltsville and Horn Point show north winds below 0.3 km, indicating stronger south wind over Horn Point while the differences were east during daytime and west or south at nighttime. This change was influenced by the occurrence of the Chesapeake Bay breeze which frequently occurs (Loughner et al., 2011). The stronger and opposing winds at Horn Point compared to Beltsville acted in such a way to block the efficient air mass advection and transport from west-to-east and lead to stagnation of smoke.

The WRF-Chem simulated winds at these three stations agree with the observed winds evolution (Fig. 7b, d, f). The wind direction, strength, and character as well as the periodicity and strength of the

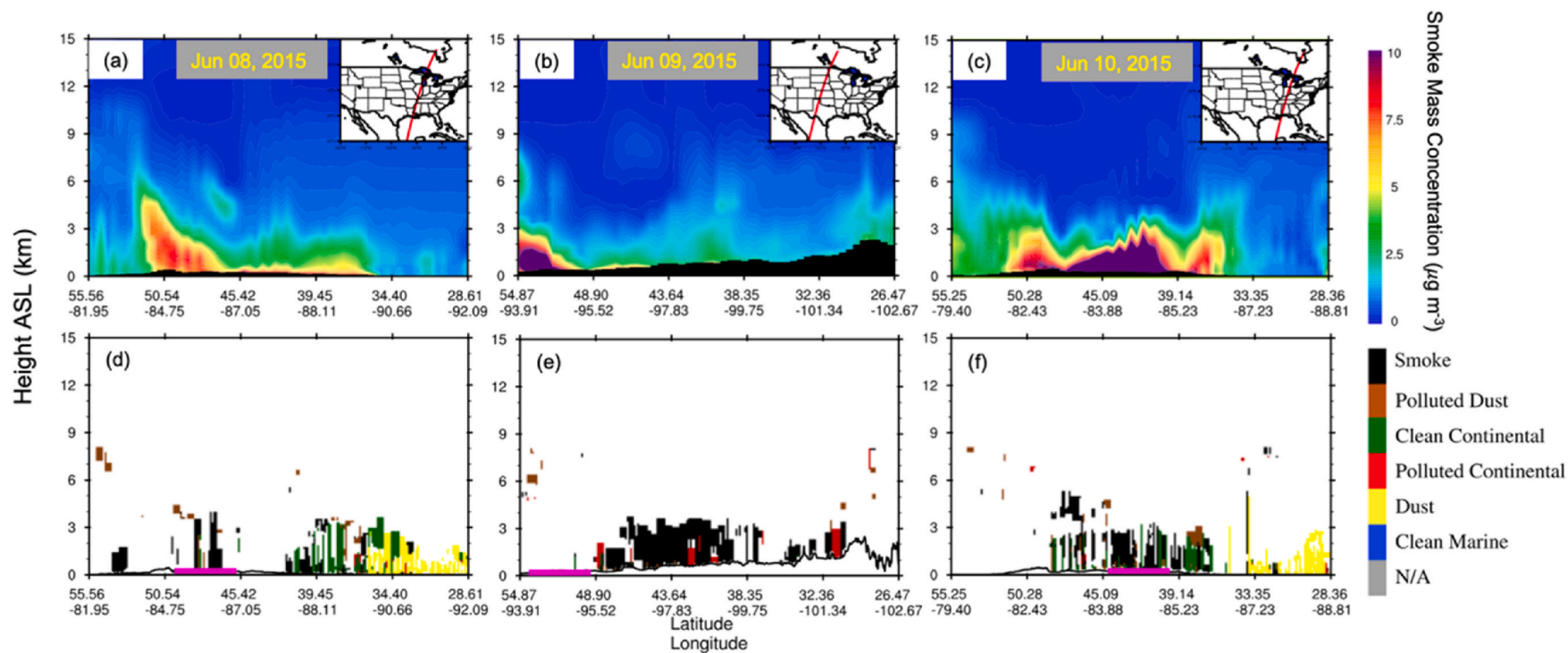


Fig. 6. Panels (a–c): WRF-Chem simulated PM_{2.5} mass concentration vertical cross section along the CALIPSO ground track. Panels (d–f): CALIOP-derived vertical feature mask. The inset on the upper right shows the CALIPSO ground track (red curve). The vertical coordinate is the height above sea level. (For interpretation of the references to color in this figure legend, the reader is referred to the Web version of this article.)

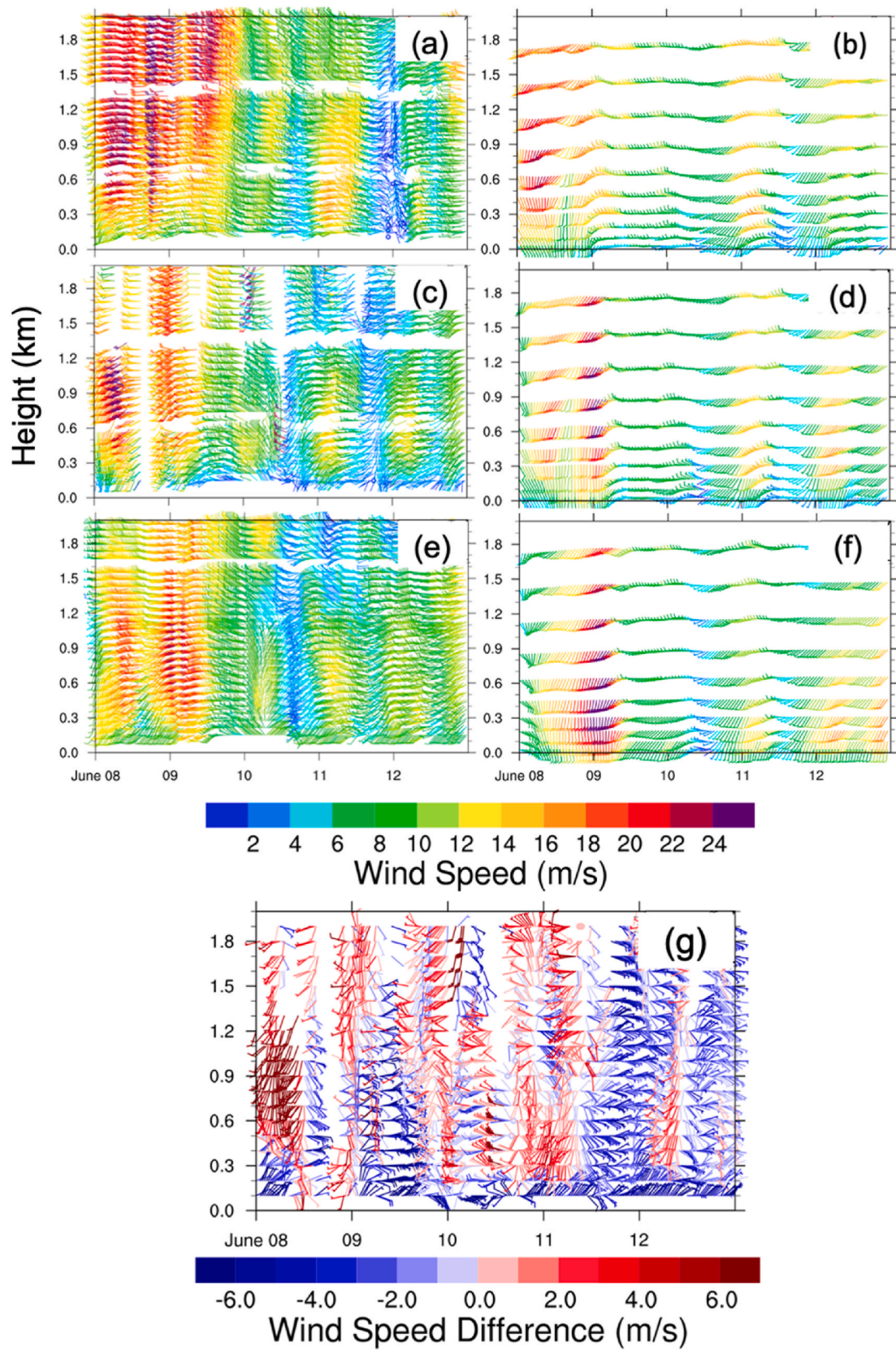


Fig. 7. 915 MHz wind radar profiler and WRF-Chem simulated horizontal wind speed and direction vertical profiles at three sites on 8–12 June 2015. (a), (c), and (e) are the wind radar observations. (b), (d), and (f) are the WRF-Chem simulation. (a) and (b), Piney Run; (c) and (d), Beltsville; (e) and (f), Horn Point; (g), wind difference between Beltsville and Horn Point.

lowest 2 km of the troposphere is simulated well and hints at a correct simulation of the smoke advection and timing. The model-observation comparison is a reason for strong confidence on the validity of the WRF-Chem smoke transport location and character used here for discussion of its impact on O₃ and PM measurements at surface and profile over the Beltsville station.

4.3.2. Surface O₃ diurnal variation

The observed and simulated surface O₃ mixing ratios show significant diurnal variations (Fig. 8). Ex1 and Ex3 simulation results were employed to analyze the impacts of smoke on the O₃ diurnal variation. The WRF-Chem model simulated surface O₃ mixing ratio was generated by averaging three by three model meshes surrounding the selected station (nine meshes in total). The TROPOZ O₃ lidar data is included for comparison purposes. This lidar profile starts at 102.5 m above ground level and has uncertainty of about 10% (Sullivan et al., 2015). What is plotted is an average of the first 10-levels of TROPOZ data (102.5–237.5 m). The larger TROPOZ data compared to AirNow surface measurements is expected as the TROPOZ O₃ profile shows O₃ mixing ratio increased from the surface to 500 m in Fig. 10d, but is indicative of near-surface O₃ concentration.

The surface O₃ diurnal evolutions on 12 June at Hagerstown, Edgewood, and Beltsville are shown in Fig. 8. The O₃ mixing ratio diurnal variability shows generally a similar pattern and the daily average values are 50–60 ppbv. At Hagerstown, the magnitude and diurnal

pattern of model simulated and AirNow observed O₃ mixing ratio diurnal variations agree well, with slight and consistent model overestimation during daytime (Fig. 8a). The model-observation Pearson correlation coefficient and root mean square error (RMSE) was 0.99 and 3.02 ppbv, respectively. At Edgewood, a well-known and significant O₃ pollution station (see Crawford and Pickering, 2014), the model simulated surface O₃ agreed well with the observed O₃, although the model simulated O₃ diurnal variation was relatively smooth. The model-observation Pearson correlation coefficient was 0.96 and RMSE was 5.96 ppbv. The daily model averaged O₃ mixing ratio was 55 ppbv. The comparison between Hagerstown and Edgewood showed the similarities and differences between two stations. The similarity was the O₃ mixing ratio diurnal variation, while the difference was the maximum O₃ mixing ratio. The daytime maximum O₃ mixing ratio was 70 ppbv at Hagerstown, while 85 ppbv at Edgewood. Another difference is the time when the maximum O₃ occurred and how long it lasted. At Hagerstown, the daytime O₃ mixing ratio was very smooth after reaching maximum at 1600 UTC and lasted until the end of day (1200 EST, Fig. 8a). However, at Edgewood, the O₃ mixing ratio reached the maximum at 1600 UTC (1200 EST) and lasted until 1800 UTC (1400 EST), then decreased from the maximum of 85 ppbv–60 ppbv (Fig. 8b).

The diurnal variation at Beltsville includes TROPOZ O₃ lidar, EPA AirNow, and simulations of Ex1 and Ex3. Ex1 simulation underestimated the O₃ mixing ratio significantly due to the lack of fire emissions. Its maximum O₃ mixing ratio was only 25 ppbv at daytime, while the TROPOZ and AirNow maximum observed O₃ mixing ratio was 120 ppbv, which is due to its suburban location. Previous studies reported that the O₃ concentration in urban regions was elevated in the presence of the wildfire smoke (Brey et al., 2016). Dreessen et al. (2016) and Sullivan et al. (2017) reported that the O₃ concentration increased after the arrival of the Canadian wildfire smoke over the Baltimore-Washington D.C. metropolis. Brey et al., (2016) reported that the enhanced O₃ was due to the mixture of O₃ precursors generated from wildfire and local NO_x emissions. After considering the FINN fire emissions, Ex3 matched the observed O₃ mixing ratio much better, but still underestimated the O₃ mixing ratio from 1500 to 1900 UTC. The Pearson correlation coefficient was 0.96, while the RMSE was 17.19 ppbv.

4.3.3. Vertical profile

In this section, the evolutions of aerosol and O₃ vertical profiles at Beltsville are discussed. We will focus on the model performance evaluation and its comparison with observations and the onset of the long-range transported smoke mixing-down into the PBL and influence on the local air quality.

4.3.3.1. Smoke vertical profile evolution. The ceilometer CL51 aerosol backscatter profiles and the WRF-Chem simulated PM_{2.5} mass concentrations of Ex1, Ex2, and Ex3 on 10–12 June are shown in Fig. 9. The plots clearly show smoke arrived on 10 June at 2–4 km and slowly descended and later mixed down into the PBL, meanwhile convective boundary layer grew, and wildfire smoke and precursors entrained into it (Fig. 9a and d). Eventually it was reported as increased BC concentration measurements reported by Dreessen et al. (2016). The elevated BC concentration was consistent with the growth of the PBL and merging with the smoke laden layer. The strength of the lidar backscatter was indicative of the increased particle concentration as it started to mix down to the PBL.

The model simulations did capture the large-scale structure revealed by the ceilometer observations: the continued descent and intrusion into the PBL and down to the surface. The model shows air was clean at low levels prior to 1600 UTC then smoke concentration increased in the afternoon on 10 June. The simulated PBL reached 2 km, where the smoke layer was located, supporting the idea that the convective overturning was responsible. While the general large-scale trend of the

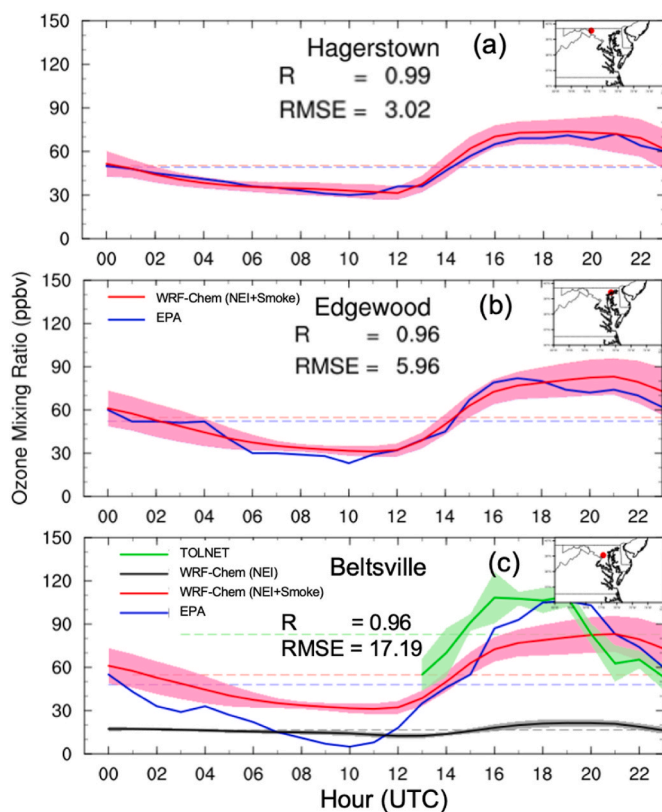


Fig. 8. Diurnal variations of the surface O₃ mixing ratio of EPA AirNow, TROPOZ and WRF-Chem simulation at sites: (a) Hagerstown (rural), (b) Edgewood (coastal), and (c) Beltsville (suburban) on June 12, 2015. The red shaded areas indicate standard deviations of the WRF-Chem simulation; and surface O₃ concentration daily averages are denoted as dashed lines. The location of the station is indicated by a red dot on a map in the upper right corner. Pearson correlation coefficients and RMSEs between EPA AirNow and WRF-Chem simulation are provided. (For interpretation of the references to color in this figure legend, the reader is referred to the Web version of this article.)

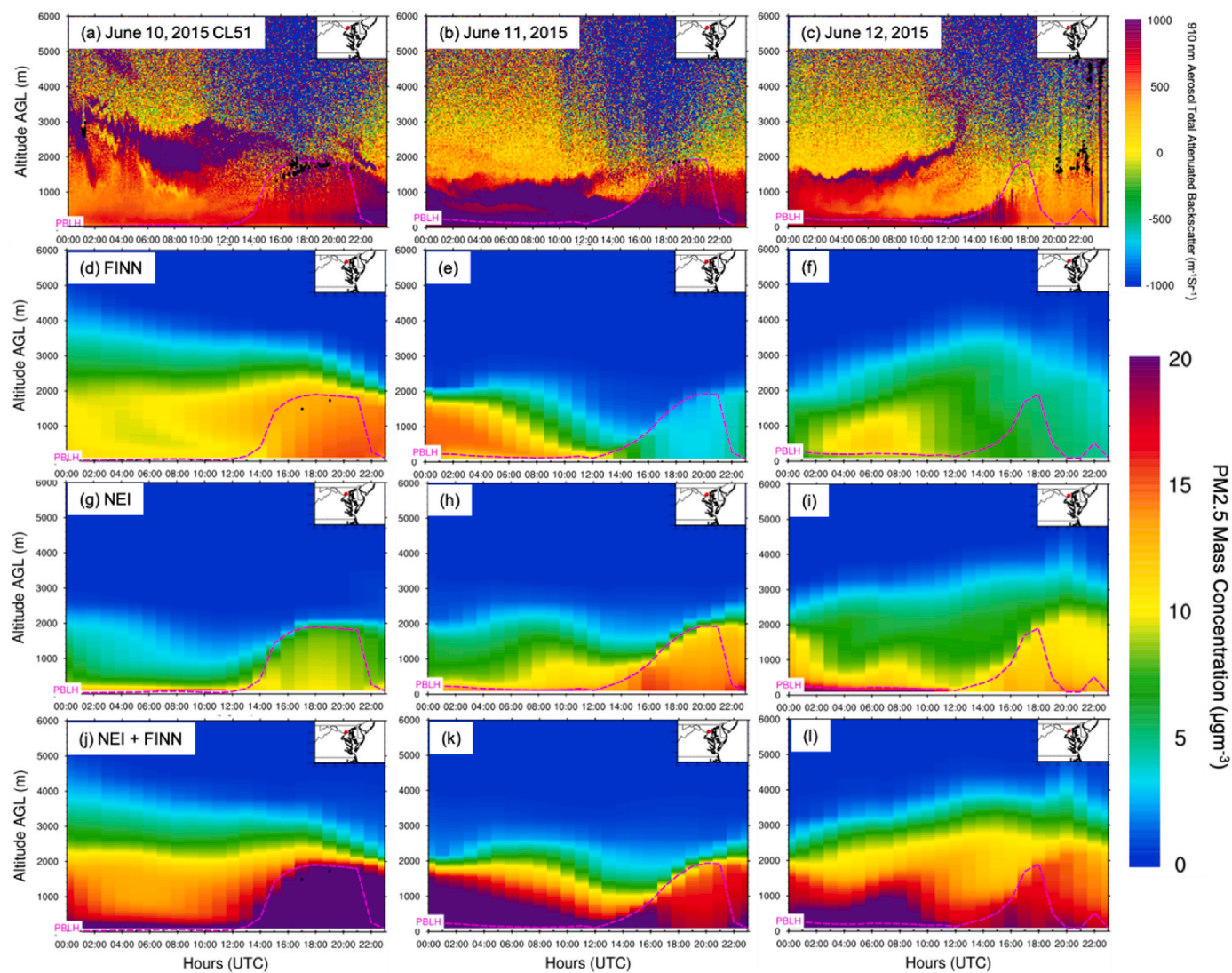


Fig. 9. Time series of ceilometer CL51 aerosol total attenuated backscatter at 910 nm (a–c) and WRF-Chem $PM_{2.5}$ mass concentration of Ex2 (d–f), Ex1 (g–i), and Ex3 (j–l) on 10–12 June 2015. The pink curve is denoted as the model simulated PBLH. The upper right inserted map shows the location of the site (red dot). (For interpretation of the references to color in this figure legend, the reader is referred to the Web version of this article.)

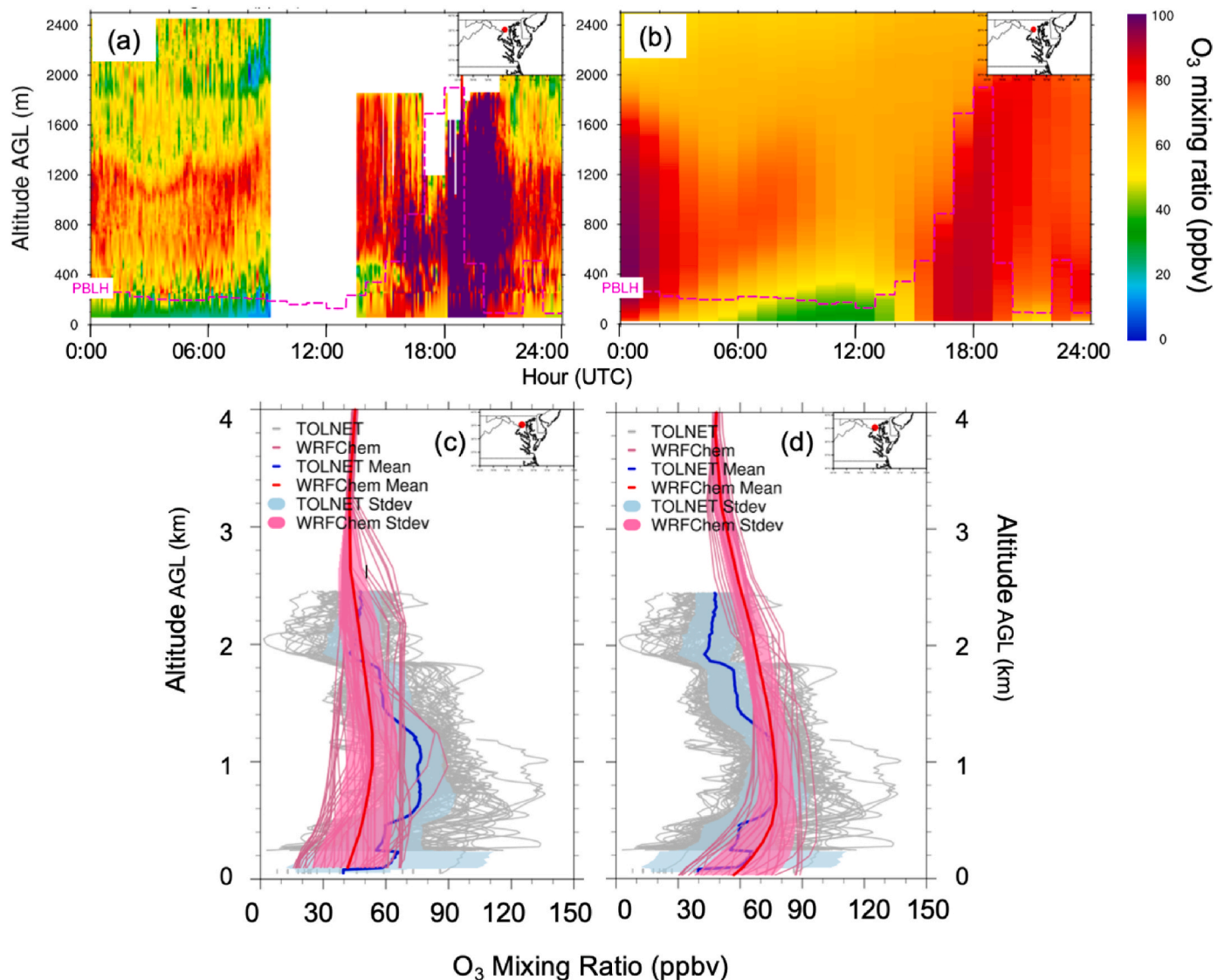


Fig. 10. O₃ mixing ratio vertical profiles from TROPOZ and WRF-Chem model on 12 June. (a) TROPOZ O₃ mixing ratio vertical profile time series and the WRF-Chem simulated PBLH (pink curve); (b) model O₃ mixing ratio vertical profile time series from Ex3; (c) Overall TROPOZ (blue and gray) and WRF-Chem (pink, Ex1) O₃ mixing ratio vertical profiles; (d) Overall TROPOZ (blue and gray) and WRF-Chem (pink, Ex3) O₃ mixing ratio vertical profiles. The upper right inserted map shows the location of the site (red dot). (For interpretation of the references to color in this figure legend, the reader is referred to the Web version of this article.)

smoke layer descent and PBL growth and decay was well simulated by the model.

The descent in altitude of the smoke layer continued on 11 June (Fig. 9b), as would be expected following the shallow nocturnal PBL development. The smoke laden air mass remained below 1 km on 11 June. Starting 0000 UTC 12 June, a clear lifting and detachment from the surface of the smoke carrying air mass was noticed. This lifting continued through the night from 1 km to 2 km by sunrise (1200 UTC) and was associated with the arrival of the air mass from the south due to increased wind speeds discussed above. The model captured the continued PBL collapse and PBL growth on 11 June and later the arrival of the air mass and associated PM_{2.5} mass concentration. It did not capture the small-scale structures, like the high aerosol concentration indicated by the ceilometer between 1 and 2 km altitude throughout the night of 12 June. The simulated PBL development on 12 June did not perform well, collapsing earlier than the previous two days.

Ex2 shows that the upper boundary of the smoke particles reached 3.5 km, consistent with the ceilometer backscattering observations (Fig. 9d). The arrival of the smoke laden air mass on 10 June, the continued descent of the layer, and the overall pattern agreed with the

observations. The nocturnal and daytime PBL development on 11 June, and the pattern of the subsequent lifting of the smoke laden air mass on 12 June were indicated in the model simulations. However, while the ceilometer data indicated a similar smoke concentration within the daytime well mixed within the PBL on 10–11 June the model indicated a much lower concentration ($5 \mu\text{g m}^{-3}$) on 11 June compared with 10 June.

Similar trends in the general descent of the atmosphere early on 10 June followed by lifting associated with air mass flow over the measurement location were shown by the simulations of Ex1 and Ex3. Ex1 did not show the level of concentrations that would indicate smoke particles (Fig. 9g, h, i). However, the model captured the surface anthropogenic pollutants below 0.2 km with concentration around $10 \mu\text{g m}^{-3}$, much lower than the smoke particle concentration. On the other hand, Ex3 shows a much better performance in matching the ceilometer observations and overall particle vertical distribution, consistent with what is expected to be contributed from smoke particles added to local pollutants (Fig. 9j).

4.3.3.2. O₃ vertical profile evolution. Along with WRF-Chem

simulations, the O₃ mixing ratio vertical profile analysis employs TROPOZ O₃ lidar measurements at the Beltsville station on 12 June, which was six days later after the wildfire event in Canada on 6 June. Fig. 10a shows TROPOZ O₃ mixing ratio measurements and the WRF-Chem simulated PBLH. No data was collected from 0900 to 1400 UTC and above cloud base. An enhanced O₃ layer (~1.2 km) at and prior to sunrise was corresponding to the elevated smoke layer (Fig. 10a). The WRF-Chem simulated O₃ mixing ratio vertical profiles at this time show an overall good agreement with the TROPOZ lidar measurement trends, including the elevated O₃ signal at 1.2 km (Fig. 10b).

The individual TROPOZ O₃ mixing ratio profiles and mean together with WRF-Chem simulated O₃ mixing ratio vertical profiles and mean are shown in Fig. 10c and d. The O₃ mixing ratio vertical profiles varied with time and altitude. The simulated O₃ mixing ratio increased from 30 to 40 ppbv near the surface to 70–80 ppbv at 1 km, followed by a smooth decrease to 50 ppbv at 3 km. The standard deviations of the simulated O₃ vertical profiles varied 5–10 ppbv. Similarly, the ozonesonde O₃ mixing ratio also increased gradually from 15 ppbv at the surface to 70 ppbv at 1.5 km, then decreased to 50 ppbv (Fig. 11). The NLLJ increased the eddy diffusivity and enhanced the turbulence, then the temperature inversion weakened. The turbulence transported O₃-rich air from the residual layer to the surface, where O₃ was efficiently removed by chemical reactions and dry deposition near the surface, which led to the lower O₃ concentration (Hu et al., 2013a,b; Sullivan et al., 2017). The model simulated PBLHs were 0.1–0.3 km (Fig. 11), which confined water vapor and chemical species vertical mixing. The WRF-Chem simulation profiles, although revealed a similar trend, were about 10 ppbv or less over the ozonesonde data. The largest difference was centered around 1–1.4 km, where the narrow wind sheared,

aerosol/smoke enhanced, layer seen in the ceilometer data above (Fig. 10c). The lidar data agreed with the ozonesonde values at about 0.3–0.5 km, the lowest available data points for lidar, and increased to 70 ppbv at 1 km, then decreased sharply to 20 ppbv at 2 km followed by an increase to almost 50 ppbv at 2.5 km. However, the WRF-Chem-TROPOZ agreement centered at 1–1.5 km was more than what the ozonesonde measured by about 15 ppbv. This difference could be caused by balloon drift out of the area due to the increased shear and wind speed present at the time. While the TROPOZ O₃ mixing ratio sharply decreased at 1.4–2 km, which was primarily caused by inability of O₃ lidar to probe in heavy aerosol and/or cloud layers because of the very low signal to noise ratio. Nevertheless, despite the elevated enhancement and the trend with altitude, the observed and simulated O₃ mixing ratios are fairly in agreement.

5. Concluding summary

This study focuses on the Canadian wildfire smoke event on June 6, 2015, and its transport pathway and influence on the local/regional air quality (O₃ and PM) in the U.S. An integrated study using WRF-Chem model simulations, ground-based observations, and satellite data identifies the source of the wildfire in Alberta and Saskatchewan provinces of Canada, the transport path through the U.S.-Canada border, the stagnation over the Ohio River Valley, and final arrival and manner of mixing to the surface over the sampling site in Beltsville, Maryland.

The FINN fire emission revealed this wildfire ejected the total PM_{2.5} area density of 100 mg m⁻² into the atmosphere and the maximum burning area was 100–150 km² per 100 km by 100 km grid on 6–8 June in Saskatchewan Province, Canada. The smoke was transported and detected over North Dakota and Minnesota on 7 June and drifted further south arriving over the Ohio River Valley by 9 June. The smoke transport path changed from south heading to east and stagnated, owing to the wind direction zonal change before it crossed the Appalachian Mountain region and started to mix-down to the surface over Beltsville late on 10 June and transported further northeast on 11–12 June. According to the smoke vertical structure, the simulated smoke vertical profiles agreed well with the CALIOP VFM measurements, both of which showed the smoke plume height around 3 km at the Mid-Atlantic.

Ground-based profile measurements of wind and O₃ were used to interrogate the model results. The radar wind profile evolution showed the temporal wind velocity vertical variation and associated diurnal cycle. On 8–12 June, the NLLJ advected pollutants to the downwind region. The model simulated wind direction and speed profiles generally agreed well with the wind radar observations, as well as diurnal cycle, which led to strong confidence on the validity of the WRF-Chem model simulated smoke transport. Surface measured O₃ diurnal variation showed that the general tendency of the WRF-Chem model simulated O₃ agreed with the EPA AirNow surface O₃. Three surface stations were selected for quantification and comparison of the modeled and measured impact by the aged smoke on the O₃ concentration, i.e., Hagerstown, Edgewood, and Beltsville. Overall, the model simulated surface O₃ diurnal variation maintained the high correlation with EPA AirNow surface O₃ observations over three stations. Their Pearson correlation coefficients were over 0.95 and RMSEs were as low as 5.0 ppbv. These results demonstrate the WRF-Chem model simulation skill and show great performance in capturing the O₃ mixing ratio diurnal variation.

Aerosol backscatter data from ceilometers revealed that transported Canadian wildfire smoke intruded into the Baltimore-Washington D.C. area from 3.5 km at 0000 UTC on 10 June. Smoke entrained to the PBL and mixed with the anthropogenic pollutants and the model experiments (Ex1 and Ex2) indicated that the smoke particle contributes about 60% to the total particle pollution. The contribution was slightly reduced the next night (~50%) attributed to the decreasing vigor in mixing and development of the shallow stable boundary layer. The role of the mixing and subsequent cleansing associated with a cold frontal

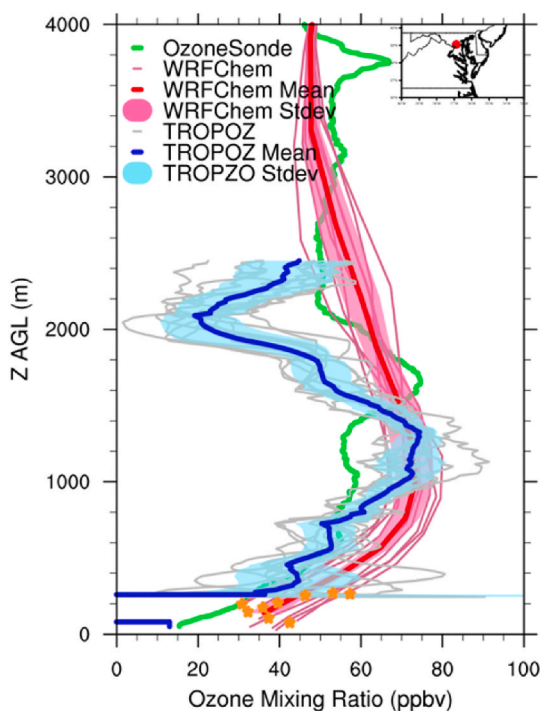


Fig. 11. O₃ mixing ratio vertical profiles of WRF-Chem (thin red curves, Ex3), ozonesonde (thick green curve), and TROPOZ O₃ lidar (thin gray curves). The WRF-Chem simulated O₃ mixing ratio profile mean and standard deviation are shown as a red thick curve and shade, respectively. The TROPOZ O₃ mixing ratio profile mean and standard deviation are shown as a blue thick curve and shade, respectively. The orange stars denote the WRF-Chem simulated PBLH for the corresponding O₃ mixing ratio profiles. The upper right inserted map shows the location of the Beltsville site (red dot). (For interpretation of the references to color in this figure legend, the reader is referred to the Web version of this article.)

passage was well captured and adequately simulated including the formation of an elevated shear-generated smoke layer.

The TROPOZ O₃ lidar observed O₃ vertical profiles at Beltsville from 1400 to 2400 UTC on 12 June matched the WRF-Chem simulated O₃ mixing ratio above 2 km well while the model underestimated the lidar data below 2 km. On the other hand, inclusion of anthropogenic, biogenic, and fire emissions (Ex3) in the simulation captured the O₃ mixing vertical profiles below 1.5 km well, compared with both TROPOZ O₃ lidar and ozonesonde observations.

Finally, this study employed the state-of-the-art lidar observed O₃ vertical profiles to evaluate the mesoscale modeling simulations of an important long-range transported smoke event. Such interrogation of model and performance in the PBL is important because of its impact on air pollution and human health. It also utilized the FINN fire emission, coupled with the anthropogenic emissions and biogenic emissions, to track and reproduce the smoke transport pathway leading to altered surface measurements. Further, by conducting three different numerical experiments, the study quantified the smoke influence on local air pollution in both O₃ and PM. However, the model simulated O₃ vertical profile did not match the O₃ lidar perfectly. In order to improve model performance on simulating the O₃ vertical profile, assimilating O₃ lidar observation into the WRF-Chem model is the future study.

Code and data availability

WRF-Chem model is publicly available at <https://www2.mmm.ucar.edu/wrf/users/>. MODIS products are publicly available at <https://atmosphere-imager.gsfc.nasa.gov/products.html>. CALIOP products can be downloaded from <https://www-calipso.larc.nasa.gov/products/inventory.php>. The EPA AirNow measurements are publicly available at <https://www.airnowtech.org/index.cfm>.

CRedit authorship contribution statement

Zhifeng Yang: designed and performed the model experiments with help from, Formal analysis, Writing – review & editing, analyzed the model results. All authors contributed to the review and editing of the paper. **Belay Demoz:** designed and performed the model experiments with help from, Formal analysis, Writing – review & editing, analyzed the model results. All authors contributed to the review and editing of the paper. **Ruben Delgado:** Formal analysis, Writing – review & editing, analyzed the model results. All authors contributed to the review and editing of the paper. **John Sullivan:** Formal analysis, Writing – review & editing, analyzed the model results. All authors contributed to the review and editing of the paper. **Andrew Tangborn:** Formal analysis, Writing – review & editing, analyzed the model results. All authors contributed to the review and editing of the paper. **Pius Lee:** analyzed the model results. All authors contributed to the review and editing of the paper.

Declaration of competing interest

The authors declare that they have no known competing financial interests or personal relationships that could have appeared to influence the work reported in this paper.

Acknowledgement

This work was partly funded by the National Science Foundation award (AGS- 1503563) to the University of Maryland, Baltimore County and by a grant from the Maryland Department of Environment (MDE) to the University of Maryland, Baltimore County. Belay Demoz and Ruben Delgado were also partially funded by the National Oceanic and Atmospheric Administration – Cooperative Science Center for Atmospheric Sciences and Meteorology (NOAA-NCAS-M) and Center for Earth System Sciences and Remote Sensing Technologies (NOAA-

CESSRST) under the Cooperative Agreement Grants #NA16SEC4810006 and #NA16SEC4810008, respectively. Belay Demoz was also funded through the Educational Partnership Program at NOAA in collaboration with Howard University. We also acknowledge the AirNow program for providing the surface O₃ observations.

References

- Andreae, M.O., Merlet, P., 2001. Emissions of trace gases and aerosols from biomass burning. *Global Biogeochem. Cycles* 15, 955–966. <https://doi.org/10.1029/2000-GB001382>.
- Brey, S.J., Fischer, E.V., 2016. Smoke in the city: how often and where does smoke impact summertime ozone in the United States? *Environ. Sci. Technol.* 50 (3), 1288–1294. <https://doi.org/10.1021/acs.est.5b05218>.
- Caicedo, V., Delgado, R., Sakai, R., Knepp, T., Williams, D., Cavender, K., Lefer, B., Szykman, J., 2020. An automated common algorithm for planetary boundary layer retrievals using aerosol lidars in support of the U.S. EPA Photochemical Assessment Monitoring Stations Program. *J. Atmos. Ocean. Technol.* 37 (10), 1847–1864. <https://doi.org/10.1175/JTECH-D-20-0050.1>.
- Campbell, J.R., Ge, C., Wang, J., Welton, E.J., Bucholtz, A., Hyer, E.J., et al., 2016. Applying advanced ground-based remote sensing in the Southeast Asian maritime continent to characterize regional proficiencies in smoke transport modeling. *J. Appl. Meteorol. Climatol.* 55 (1), 3–22. <https://doi.org/10.1175/JAMC-D-15-0083.1>.
- Canadian Interagency Forest Fire Centre. <http://www.cifcc.ca>. (Accessed 10 August 2020).
- Carroll, B.J., Demoz, B.B., Delgado, R., 2019. An overview of low-level jet winds and corresponding mixed layer depths during PECAN. *J. Geophys. Res. Atmos.* 124 (16), 9141–9160. <https://doi.org/10.1029/2019JD030658>.
- Chen, H., Burnett, R.T., Copes, R., Kwong, J.C., Villeneuve, P.J., Goldberg, M.S., et al., 2016. Ambient fine particulate matter and mortality among survivors of myocardial infarction: population-based cohort study. *Environ. Health Perspect.* 124 (9), 1421–1428. <https://doi.org/10.1289/EHP185>.
- Chen, F., Dudhia, J., 2001. Coupling an advanced land surface–hydrology model with the Penn State–NCAR MM5 modeling system. Part I: model implementation and sensitivity. *Mon. Weather Rev.* 129 (4), 569–585. [https://doi.org/10.1175/1520-0493\(2001\)129<0569:CAALSH>2.0.CO;2](https://doi.org/10.1175/1520-0493(2001)129<0569:CAALSH>2.0.CO;2).
- Chen, H., Zhang, Z., van Donkelaar, A., Bai, L., Martin, R.V., Lavigne, E., et al., 2020. Understanding the joint impacts of fine particulate matter concentration and composition on the incidence and mortality of cardiovascular disease: a component-adjusted approach. *Environ. Sci. Technol.* 54 (7), 4388–4399. <https://doi.org/10.1021/acs.est.9b06861>.
- Colarco, P.R., Schoeberl, M.R., Doddridge, B.G., Marufu, L.T., Torres, O., Welton, E.J., 2004. Transport of smoke from Canadian forest fires to the surface near Washington, DC: injection height, entrainment, and optical properties. *J. Geophys. Res. Atmos.* 109 (D6). <https://doi.org/10.1029/2003JD004248>.
- Crawford, J.H., Pickering, K.E., 2014. DISCOVER-AQ: advancing strategies for air quality observations in the next decade. *Environ. Manage.* 4–7.
- Crutzen, P.J., Heidt, L.E., Krasnec, J.P., Pollock, W.H., Seiler, W., 1979. Biomass burning as a source of atmospheric gases CO, H₂, N₂O, NO, CH₃Cl and COS. *Nature* 282 (5736), 253. <https://doi.org/10.1038/282253a0>.
- Crutzen, P.J., Andreae, M.O., 1990. Biomass burning in the tropics: impact on atmospheric chemistry and biogeochemical cycles. *Science* 250 (4988), 1669–1678. <https://doi.org/10.1126/science.250.4988.1669>.
- DeBell, L.J., Talbot, R.W., Dibb, J.E., Munger, J.W., Fischer, E.V., Frohling, S.E., 2004. A major regional air pollution event in the northeastern United States caused by extensive forest fires in Quebec, Canada. *J. Geophys. Res. Atmos.* 109 (D19). <https://doi.org/10.1029/2004JD004840>.
- Dreessen, J., Sullivan, J., Delgado, R., 2016. Observations and impacts of transported Canadian wildfire smoke on ozone and aerosol air quality in the Maryland region on June 9–12, 2015. *J. Air Waste Manag. Assoc.* 66 (9), 842–862. <https://doi.org/10.1080/10962247.2016.1161674>.
- Dye, T., Chan, A., Anderson, C.B., Strohm, D., Wayland, R., White, J., 12-16 January 2004. From raw air quality data to the nightly news: an overview of how EPA's AirNow program operates. In: Sixth Conference on Atmospheric Chemistry. American Meteorological Society annual meeting, Seattle, Washington, United States.
- Ecklund, W.L., Carter, D.A., Balsley, B.B., 1988. A UHF wind profiler for the boundary layer: brief description and initial results. *J. Atmos. Ocean. Technol.* 5 (3), 432–441. [https://doi.org/10.1175/1520-0426\(1988\)005<0432:AUWPF>2.0.CO;2](https://doi.org/10.1175/1520-0426(1988)005<0432:AUWPF>2.0.CO;2).
- Fast, J.D., Gustafson Jr., W.I., Easter, R.C., Zaveri, R.A., Barnard, J.C., Chapman, E.G., et al., 2006. Evolution of ozone, particulates, and aerosol direct radiative forcing in the vicinity of Houston using a fully coupled meteorology-chemistry-aerosol model. *J. Geophys. Res. Atmos.* 111 (D21). <https://doi.org/10.1029/2005JD006721>.
- Freeborn, P.H., Wooster, M.J., Roy, D.P., Cochrane, M.A., 2014. Quantification of MODIS fire radiative power (FRP) measurement uncertainty for use in satellite-based active fire characterization and biomass burning estimation. *Geophys. Res. Lett.* 41 (6), 1988–1994. <https://doi.org/10.1002/2013GL059086>.
- Gan, R.W., Liu, J., Ford, B., O'Dell, K., Vaidyanathan, A., Wilson, A., Volckens, J., Pfister, G., Fischer, E.V., Pierce, J.R., Magzamen, S., 2020. The association between wildfire smoke exposure and asthma-specific medical care utilization in Oregon during the 2013 wildfire season. *J. Expo. Sci. Environ. Epidemiol.* <https://doi.org/10.1038/s41370-020-0210-x>.

- Gillett, N.P., Weaver, A.J., Zwiers, F.W., Flannigan, M.D., 2004. Detecting the effect of climate change on Canadian forest fires. *Geophys. Res. Lett.* 31 <https://doi.org/10.1029/2004GL020876>. L18211.
- Grell, G., Freitas, S.R., Stuefer, M., Fast, J., 2011. Inclusion of biomass burning in WRF-Chem: impact of wildfires on weather forecasts. *Atmos. Chem. Phys.* 11 (11) <https://doi.org/10.5194/acp-11-5289-2011>.
- Grell, G.A., Peckham, S.E., Schmitz, R., McKeen, S.A., Frost, G., Skamarock, W.C., Eder, B., 2005. Fully coupled online chemistry within the WRF model. *Atmos. Environ.* 39, 6957–6975. <https://doi.org/10.1016/j.atmosenv.2005.04.027>.
- Guenther, A., Karl, T., Harley, P., Wiedinmyer, C., Palmer, P.I., Geron, C., 2006. Estimates of global terrestrial isoprene emissions using MEGAN (model of emissions of gases and aerosols from nature). *Atmos. Chem. Phys.* 6 (11), 3181–3210.
- Hao, Y., Balluz, L., Strosnider, H., Wen, X.J., Li, C., Qualters, J.R., 2015. Ozone, fine particulate matter, and chronic lower respiratory disease mortality in the United States. *Am. J. Respir. Crit. Care Med.* 192 (3), 337–341. <https://doi.org/10.1164/rccm.201410-1852OC>.
- Hong, S.Y., Pan, H.L., 1996. Nonlocal boundary layer vertical diffusion in a medium-range forecast model. *Mon. Weather Rev.* 124, 2322–2339. [https://doi.org/10.1175/1520-0493\(1996\)124<2322:NBLVDI>2.0.CO;2](https://doi.org/10.1175/1520-0493(1996)124<2322:NBLVDI>2.0.CO;2).
- Hong, S.Y., Noh, Y., Dudhia, J., 2006. A new vertical diffusion package with an explicit treatment of entrainment processes. *Mon. Weather Rev.* 134, 2318–2341. <https://doi.org/10.1175/MWR3199.1>.
- Hu, X.M., Klein, P.M., Xue, M., Zhang, F., Doughty, D.C., Forkel, R., et al., 2013a. Impact of the vertical mixing induced by low-level jets on boundary layer ozone concentration. *Atmos. Environ.* 70, 123–130. <https://doi.org/10.1016/j.atmosenv.2012.12.046>.
- Hu, X.M., Klein, P.M., Xue, M., 2013b. Evaluation of the updated YSU planetary boundary layer scheme within WRF for wind resource and air quality assessments. *J. Geophys. Res. Atmos.* 118 (18) <https://doi.org/10.1002/jgrd.50823>.
- Iacono, M.J., Delamere, J.S., Mlawer, E.J., Shephard, M.W., Clough, S.A., Collins, W.D., 2008. Radiative forcing by long-lived greenhouse gases: calculations with the AER radiative transfer models. *J. Geophys. Res.* 113 <https://doi.org/10.1029/2008JD009944>. D13103.
- IPCC, 2013. *Climate Change 2013: the Physical Science Basis. Contribution of Working Group I to the Fourth Assessment. Report of the Intergovernmental Panel on Climate Change.* Cambridge University Press, Cambridge, United Kingdom and New York, NY, USA, p. 1552.
- Jaffe, D.A., Wigder, N.L., 2012. Ozone production from wildfires: a critical review. *Atmos. Environ.* 51, 1–10. <https://doi.org/10.1016/j.atmosenv.2011.11.063>.
- Kain, J.S., 2004. The Kain-Fritsch convective parameterization: an update. *J. Appl. Meteorol.* 43, 170–181. [https://doi.org/10.1175/1520-0450\(2004\)043<0170:TKCPAU>2.0.CO;2](https://doi.org/10.1175/1520-0450(2004)043<0170:TKCPAU>2.0.CO;2).
- Kain, J.S., Fritsch, J.M., 1990. A one-dimensional entraining/detraining plume model and its application in convective parameterization. *J. Atmos. Sci.* 47, 2784–2802. [https://doi.org/10.1175/1520-0469\(1990\)047<2784:AODEPM>2.0.CO;2](https://doi.org/10.1175/1520-0469(1990)047<2784:AODEPM>2.0.CO;2).
- Komhyr, W.D., Barnes, R.A., Brothers, G.B., Lathrop, J.A., Opperman, D.P., 1995. Electrochemical concentration cell ozonesonde performance evaluation during STOIIC 1989. *J. Geophys. Res.* 100, 9231–9244. <https://doi.org/10.1029/94JD02175>.
- Kunzli, N., Avol, E., Wu, J., Gauderman, W.J., Rappaport, E., Millstein, J., 2006. Health effects of the 2003 Southern California wildfires on children. *Am. J. Respir. Crit. Care Med.* 174, 1221–1228. <https://doi.org/10.1164/rccm.200604-5190C>.
- Kusaka, H., Kondo, H., Kikigawa, Y., Kimura, F., 2001. A simple single-layer urban canopy model for atmospheric models: comparison with multi-layer and slab models. *Boundary-Layer Meteorol.* 101 (3), 329–358. <https://doi.org/10.1023/A:1019207923078>.
- Levy, R., 2015. Co-Authors: MODIS Atmosphere L2 Aerosol Product. NASA MODIS Adaptive Processing System. Goddard Space Flight Center, USA.
- Lippmann, M., 1991. Health effects of tropospheric ozone. *Environ. Sci. Technol.* 25, 1954–1962. <https://doi.org/10.1021/es00180a002>.
- Liu, Y., Stanturf, J., Goodrick, S., 2010. Trends in global wildfire potential in a changing climate. *For. Ecol. Manag.* 259 (4), 685–697. <https://doi.org/10.1016/j.foreco.2009.09.002>.
- Liu, Z., Vaughan, M., Winker, D., Hostetler, C., Poole, L., Hlavka, D., Hart, W., McGill, M., 2004. Use of probability distribution functions for discriminating between cloud and aerosol in lidar backscatter data. *J. Geophys. Res. Atmos.* 109 (D15) <https://doi.org/10.1029/2004JD004732>.
- Lopez-Coto, I., Hicks, M., Karion, A., Sakai, R., Demoz, B., Prasad, K., Whetstone, J., 2020. Assessment of Planetary Boundary Layer Parameterizations and Urban Heat Island Comparison: Impacts and Implications for Tracer Transport. *J. Appl. Meteorol. Climatol.* 59 (10), 1637–1653. <https://doi.org/10.1175/JAMC-D-19-0168.1>.
- Loughner, C.P., Allen, D.J., Pickering, K.E., Zhang, D.L., Shou, Y.X., Dickerson, R.R., 2011. Impact of fair-weather cumulus clouds and the Chesapeake Bay breeze on pollutant transport and transformation. *Atmos. Environ.* 45 (24), 4060–4072. <https://doi.org/10.1016/j.atmosenv.2011.04.003>.
- McKeen, S.A., Wotawa, G., Parrish, D.D., Holloway, J.S., Buhr, M.P., Hübler, G., et al., 2002. Ozone production from Canadian wildfires during June and July of 1995. *J. Geophys. Res. Atmos.* 107 (D14) <https://doi.org/10.1029/2001JD000697>.
- Milford, J.B., Russell, A.G., Mcrae, G.J., 1989. A new approach to photochemical pollution-control: implications of spatial patterns in pollutant responses to reductions in nitrogen-oxides and reactive organic gas emissions. *Environ. Sci. Technol.* 23 (10), 1290–1301. <https://doi.org/10.1021/es00068a017>.
- Morris, G.A., Hersey, S., Thompson, A.M., Pawson, S., Nielsen, J.E., Colarco, P.R., et al., 2006. Alaskan and Canadian forest fires exacerbate ozone pollution over Houston, Texas, on 19 and 20 July 2004. *J. Geophys. Res. Atmos.* 111 (D24) <https://doi.org/10.1029/2006JD007090>.
- Newchurch, M.J., Kuang, S., Leblanc, T., Alvarez, R.J., Langford, A.O., Senff, C.J., et al., 2016. TOLNET-A tropospheric ozone lidar profiling network for satellite continuity and process studies. In: EPJ Web of Conferences, vol. 119. EDP Sciences, 20001. <https://doi.org/10.1051/epjconf/201611920001>.
- Omar, A.H., Winker, D.M., Vaughan, M.A., Hu, Y., Trepte, C.R., Ferrare, R.A., et al., 2009. The CALIPSO automated aerosol classification and lidar ratio selection algorithm. *J. Atmos. Ocean. Technol.* 26 (10), 1994–2014. <https://doi.org/10.1175/2009JTECHA1231.1>.
- Peterson, D., Wang, J., Ichoku, C.M., Hyer, E., Ambrosia, V., 2013. A sub-pixel-based calculation of fire radiative power from MODIS observations: 1 Algorithm development and initial assessment. *Remote Sens. Environ.* 129, 262–279. <https://doi.org/10.1016/j.rse.2012.10.036>.
- Power, M.C., Adar, S.D., Yanosky, J.D., Weuve, J., 2016. Exposure to air pollution as a potential contributor to cognitive function, cognitive decline, brain imaging, and dementia: a systematic review of epidemiologic research. *Neurotoxicology* 56, 235–253. <https://doi.org/10.1016/j.neuro.2016.06.004>.
- Roberts, J., Trainer, M., Murphy, D., Brown, S., Brewer, A., Gao, R.S., Fahey, D., 2019. Fire influence on regional to global environments and air quality (FIREX-AQ). Available online: <https://www.esrl.noaa.gov/csd/projects/firex-aq/whitepaper.pdf>. (Accessed 20 July 2020).
- Schoennagel, T., Balch, J.K., Brenkert-Smith, H., Dennison, P.E., Harvey, B.J., Krawchuk, M.A., et al., 2017. Adapt to more wildfire in western North American forests as climate changes. *Proc. Natl. Acad. Sci. Unit. States Am.* 114 (18), 4582–4590. <https://doi.org/10.1073/pnas.1617464114>.
- Stanaway, J.D., Afshin, A., Gakidou, E., Lim, S.S., Abate, D., Abate, K.H., et al., 2018. Global, regional, and national comparative risk assessment of 84 behavioural, environmental and occupational, and metabolic risks or clusters of risks for 195 countries and territories, 1990–2017: a systematic analysis for the Global Burden of Disease Study 2017. *Lancet* 392 (10159), 1923–1994. [https://doi.org/10.1016/S0140-6736\(18\)32225-6](https://doi.org/10.1016/S0140-6736(18)32225-6).
- Sullivan, J.T., 2015. Improving the Current Understanding of the Evolution and Vertical Processes of Tropospheric Ozone Using a Ground Based Differential Absorption Lidar. University of Maryland, Baltimore County.
- Sullivan, J.T., Rabenhorst, S.D., Dreessen, J., McGee, T.J., Delgado, R., Twigg, L., Sumnicht, G., 2017. Lidar observations revealing transport of O₃ in the presence of a nocturnal low-level jet: regional implications for “next-day” pollution. *Atmos. Environ.* 158, 160–171. <https://doi.org/10.1016/j.atmosenv.2017.03.039>.
- Thompson, G., Rasmussen, R.M., Manning, K., 2004. Explicit forecasts of winter precipitation using an improved bulk microphysics scheme. Part I: description and sensitivity analysis. *Mon. Weather Rev.* 132 (2), 519–542. [https://doi.org/10.1175/1520-0493\(2004\)132<0519:EFOWPU>2.0.CO;2](https://doi.org/10.1175/1520-0493(2004)132<0519:EFOWPU>2.0.CO;2).
- Val Martin, M., Honrath, R.E., Owen, R.C., Pfister, G., Fialho, P., Barata, F., 2006. Significant enhancements of nitrogen oxides, black carbon, and ozone in the North Atlantic lower free troposphere resulting from North American boreal wildfires. *J. Geophys. Res. Atmos.* 111 (D23) <https://doi.org/10.1029/2006JD007530>.
- Westerling, A.L., Hidalgo, H.G., Cayan, D.R., Swetnam, T.W., 2006. Warming and earlier spring increases western US forest wildfire activity. *Science* 313, 940–943. <https://doi.org/10.1126/science.1128834>.
- Wiedinmyer, C., Akagi, S., Yokelson, R., Emmons, L., Al-Saadi, J., Soja, A., 2011. The Fire Inventory from NCAR (FINN): a high resolution global model to estimate the emissions from open burning. *Geosci. Model Dev.* 4, 625–641. <https://doi.org/10.5194/gmd-4-625-2011>.
- Wiedinmyer, C., Quayle, B., Geron, C., Belote, A., McKenzie, D., Zhang, X., O'Neill, S., Klos Wynne, K., 2006. Estimating emissions from fires in North America for air quality modeling. *Atmos. Environ.* 40, 3419–3432. <https://doi.org/10.1016/j.atmosenv.2006.02.010>.
- Winker, D., Vaughan, M., Omar, A., Hu, Y., Kathleen, P., Liu, Z., Hunt, W., Stuart, Y., 2009. Overview of the CALIPSO Mission and CALIOP Data Processing Algorithms. *J. Atmos. Ocean. Technol.* 26 (11), 2310–2323. <https://doi.org/10.1175/2009JTECHA1281.1>.
- Wotawa, G., Trainer, M., 2000. The influence of Canadian forest fires on pollutant concentrations in the United States. *Science* 288 (5464), 324–328. <https://doi.org/10.1126/science.288.5464.324>.
- Wu, Y., Arapi, A., Huang, J., Gross, B., Moshary, F., 2018. Intra-continental wildfire smoke transport and impact on local air quality observed by ground-based and satellite remote sensing in New York City. *Atmos. Environ.* 187, 266–281. <https://doi.org/10.1016/j.atmosenv.2018.06.006>.
- Zaveri, R.A., Peters, L.K., 1999. A new lumped structure photochemical mechanism for large-scale applications. *J. Geophys. Res.* 104, 30387–30415. <https://doi.org/10.1029/1999JD900876>.
- Yang, Z., Wang, J., Ichoku, C., Hyer, E., Zeng, J., 2013. Mesoscale modeling and satellite observation of transport and mixing of smoke and dust particles over northern sub-Saharan African region. *J. Geophys. Res. Atmos.* 118 <https://doi.org/10.1002/2013JD020644>.
- Zaveri, R.A., Easter, R.C., Fast, J.D., Peters, L.K., 2008. Model for simulating aerosol interactions and chemistry (MOSAIC). *J. Geophys. Res.* 113, D13204 <https://doi.org/10.1029/2007JD008782>.